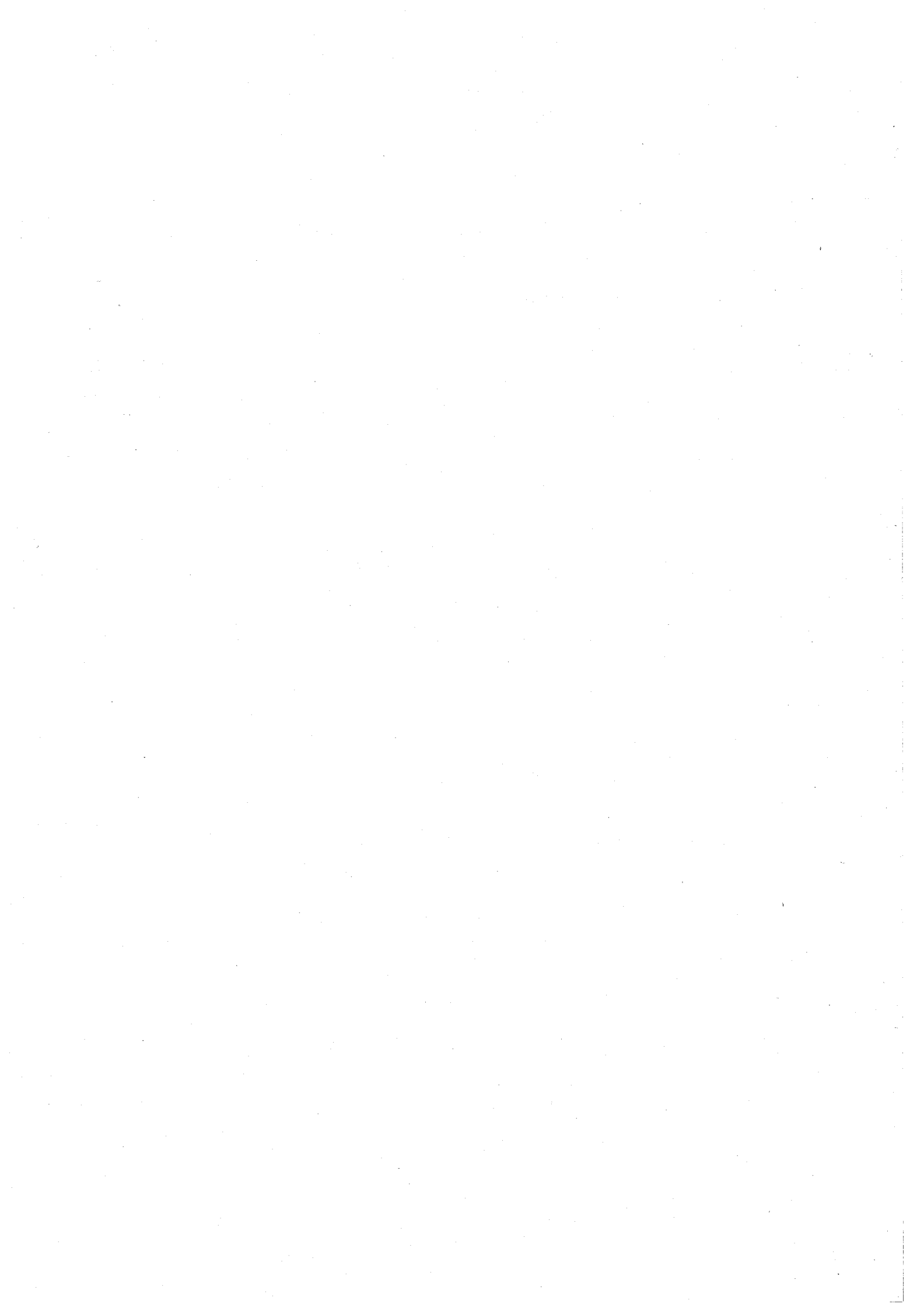


# 1. Ion Implantation Doping and Gate Insulators of GaN

(GaNへのイオン注入によるドーピング  
及びゲート絶縁膜に関する研究)



# Chapter 1

## Introduction

### 1.1 Background

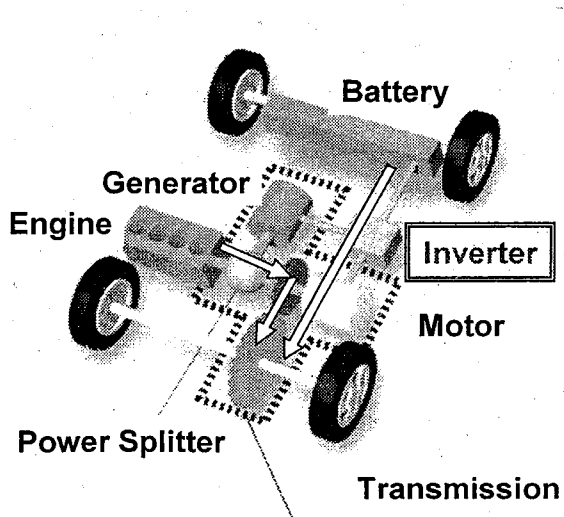
Power semiconductor devices play a crucial role in the regulation and distribution of power and energy in the world. The 21<sup>st</sup> highly-networked information society typified by information technology (IT) is estimated to use much more electric power than the 20<sup>th</sup> century, in all aspects such as energy flow, information flow, and materials flow. The demand of electric power which is clean and user-friendly tends to be proportional to the GNP (gross national product), and electric power conversion from energy becomes distinguished all over the world. The power conversion efficiency from primary energy has been already achieved at a level of ~40 % in advanced countries such as USA and Japan. Furthermore, in the advanced countries, the conversion efficiency is also estimated to increase more than ever, in accordance with the advance in IT and the popularization of electric vehicles (EV), hybrid electric vehicles (HEV), and fuel cell vehicles (FCV). From a viewpoint of global environment, the total conversion efficiency may attain a level of ~50 % in the middle of the 21<sup>st</sup> century. Thus, power electronics as a means to control electrical energy will show more and more increasing importance in refining and innovating the social infrastructure in the 21<sup>st</sup> century of full-blown electric epoch. Up to date, power switching devices which act as a core technology of the power electric system have been fabricated from Si semiconductor, and Si has long been the dominant semiconductor of choice for high-power devices. Additionally, it is well recognized that the improvements in system performance in term of efficiency, size, and weight, are driven by enhancements made in power device characteristics. Power devices used in the power electric system can be broadly classified into two categories; power rectifiers and power switches. Recently, Si-based power devices encounter its theoretical

limitation due to its material properties. In Si power devices, power output under a high-frequency operation is not so high due to power loss consisting of conduction loss and switching loss. In order to minimize the power loss in Si power devices, there has been a concerned effort to reduce on-resistance by increasing the device die area. In high-frequency applications, as the die size increases, an increase in input capacitance produces a corresponding increase in switching loss that offsets a reduction in conduction loss achieved by a decrease in on-resistance. Thus, it is necessary to reduce the specific on-resistance to keep the die size for small input capacitance. At the same time, to break through the material limits of Si and to realize a drastic performance improvement needed to meet the severe requirements in the future, wide bandgap semiconductors such as SiC, GaN, and diamond, have attracted much attention because of their superior material properties. Thus, new functional power devices based on wide bandgap semiconductors will be desirable, and might be expected to operate the electric power with high efficiency, instead of the Si power devices.

## 1.2 Prospects of GaN Power Devices in EV Electronics

Switching gear to EV electronic applications, nowadays, some kinds of HEV, equipped with a gasoline engine and an electric motor, start to be commercialized. In the commercialized HEV, driving energy flows from both an engine and a battery, as shown in Fig. 1.1. In the near future, we have to develop the zero emission vehicles, because low emission is strongly required for environmental protection. Here, an ideal vehicle is thought to be a pure EV and/or a FCV. In the pure EV and FCV, a motor and an inverter correspond to an engine of the present automobile. The motor performance is now superior to the inverter performance. As a consequence, the driving performance of HEV, EV, and FCV is limited by the inverter performance. Thus, the inverter performance needs to be better improved. However, there are some development issues of power devices for EV electronic systems; low cost, high current density ( $> 300 \text{ A/cm}^2$ ), high blocking voltage ( $\sim 1000 \text{ V}$ ), high operation temperature ( $\sim 200^\circ\text{C}$ ), high efficiency from low output to maximum output (monopolar device), and high reliability (gate oxide, solder, etc, for 15 years). As

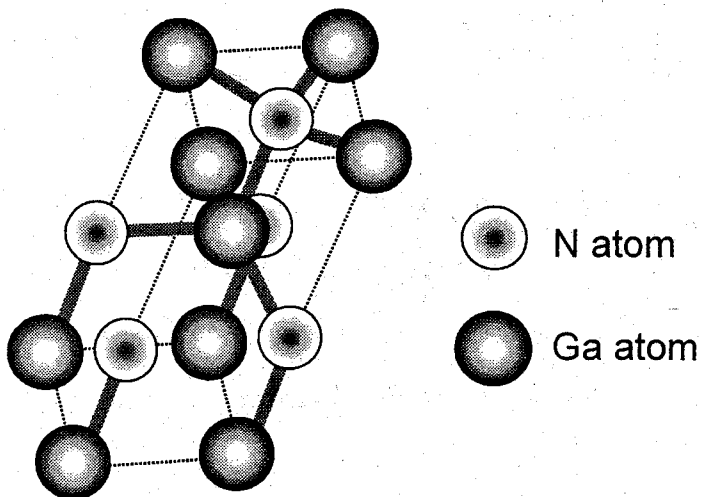
described in section 1.1, Si-based power devices are rapidly approaching the theoretical limits of performance. Thus, we need to investigate new materials instead of Si. Wide bandgap semiconductors such as SiC, GaN, and diamond, are most promising for this application, because they offer several potential advantages over Si-based power devices in the areas of switching (faster with lower power loss), operating temperature, and blocking voltage. Unique material properties such as wide bandgap, high electric breakdown field, and high saturated electron velocity give these materials their tremendous potential, as described later.



**FIG. 1.1** A schematic of HEV system.

In general, GaN have Wurtzite and Zincblende polytypes. The prospective polytype for power devices is Wurtzite GaN, as shown in Fig. 1.2, because the bandgap of Wurtzite GaN is much larger than that of Zincblende GaN. Wurtzite GaN has recently attracted increasing interest for applications in high-temperature and high-power electronics due to the outstanding features, as summarized in Table 1.1 [1-4]. The first feature is a wide bandgap of 3.39 eV, which is about three times larger than that of Si. The wide bandgap of GaN results in a very low intrinsic carrier concentration  $n_i$  of  $1.9 \times 10^{10} \text{ cm}^{-3}$  that gives negligible junction leakage current up to 500 °C. This allows high-temperature operation without excessive

leakage or thermal runaway and reduces cooling requirements, as well as 4H-SiC. The second attractive feature is a high breakdown field of  $4 \times 10^6$  V/cm, which is about one order of magnitude larger than that of Si. The high breakdown field strength requires thinner drift layers for a given blocking voltage, as compared to Si, thus reducing the specific on-resistance and storage of minority carriers. Then, in addition to a decrease in conduction loss, the associated switching loss is reduced, which enables higher switching frequency of the devices and significantly reduces the size and weight in the magnetic components in power switches. Figure 1.3 shows a plot of avalanche and punch through breakdown of GaN Schottky diodes calculated as a function of doping concentration and standoff layer thickness. It can be seen that a 1 kV device is obtained with 5- $\mu\text{m}$ -thick GaN layer with a doping concentration of  $4.6 \times 10^{16}$  cm<sup>-3</sup>. The third feature is a high saturated drift velocity of  $3.0 \times 10^7$  cm/s, which is about three times larger than Si. This excellent transport property determines the limit for high frequency operation. Thus, these material properties make GaN suitable for high-temperature, high-power, and high-frequency electronic applications. In particular, GaN power devices can be expected to operate with power loss of 1/100 and to downsize 10 times smaller compared to Si power devices.

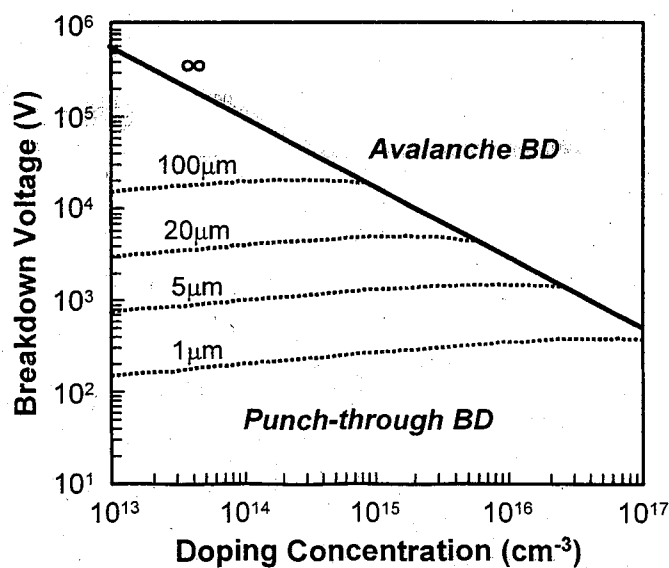


**FIG 1.2.** Unit cell of Wurzite GaN structure.

**TABLE 1.1.** Comparison of semiconductor material properties at 300K.

Property	Si	GaAs	4H-SiC	GaN
Bandgap $E_g$ (eV)	1.12	1.42	3.25	3.39
Breakdown Field $E_B$ (MV/cm)	0.25	0.4	3.0	4.0
Electron Mobility $\mu$ ( $\text{cm}^2/\text{V}\cdot\text{s}$ )	1350	6000	800	1300
Maximum Velocity $v_s$ ( $10^7 \text{ cm/s}$ )	1.0	2.0	2.0	3.0
Thermal Conductivity $\chi$ (W/cm·K)	1.5	0.5	4.9	1.3
Dielectric Constant $\epsilon$	11.8	12.8	9.7	9.0
CFOM= $\chi\epsilon\mu v_s E_B^2 / (\chi\epsilon\mu v_s E_B^2)_{\text{Si}}$	1	8	458	489

\* CFOM: Combined Figure of Merit for high-temperature/high-power/high-frequency applications

**FIG 1.3.** Calculated breakdown voltage as a function of doping concentration and thickness of the drift region in GaN Schottky diodes.

### 1.3 GaN and Related III-Nitrides for Device Applications

GaN and related III-nitride material systems (InN and AlN) have been viewed as highly promising for optoelectronic device applications at blue and ultraviolet wavelengths [5-12]. As members of the III-nitride family, AlN, GaN, InN, and their alloys are all wide bandgap semiconductor materials, and can be crystallized in both Wurtzite and Zincblende polytypes. In particular, Wurzite GaN, AlN, and InN have direct bandgaps of 3.39, 6.2, and 0.7-1.9 eV at room temperature, respectively. From a viewpoint of available wide range of direct bandgap energies, GaN alloyed with AlN and InN spans a continuous range of direct bandgap energies throughout much of the visible spectrum well into the ultraviolet wavelengths. Thus, these III-nitride systems become attractive for light emitting diodes (LEDs) [5-11], laser diodes (LDs) [12], and detectors, which are active in the green, blue, or ultraviolet wavelengths.

Substantial research on III-nitrides growth was initiated in early 1960s. However, they have trailed way behind the easier-to-grow Si and GaAs semiconductors. Nearly 30 years, Si and GaAs have been pushed to their theoretical limits, while III-nitrides have been just beginning to show their prospect. The technological spin-offs came late, because ideal substrates could not be found and consequently the grown GaN thin films contained substantial concentration of defects and had high n-type background. In addition, even in GaN films having relatively small background electron concentration, p-type doping could not be achieved until 1990s. Thus, in the past, the poor quality of the materials, the lack of p-type doping, and the absence of reliable processing procedures, thwarted engineers and scientists from fabricating these useful devices. However, the 1990s have brought significant advances in the sophistication of growth techniques, the purity of the chemicals used for film deposition, the controlled introduction and activation of selected impurities, and progress in processing techniques. Most of the aforementioned obstacles have been overcome, and the optical devices have been demonstrated and partially commercialized. From materials science to device engineering, III-nitride technologies have shown a late but exciting development.

The growth of GaN thin films is difficult due to the unavailability of sufficiently large single crystals for use as substrate for homoepitaxial growth. Thus, up to now, heteroepitaxial growth has been a practical

necessity and the choice of substrate is critical. Possible substrate materials should have low thermal expansion and lattice mismatch with the grown crystals. Also, they should be unaffected by the growth chemistries such as NH<sub>3</sub> and H<sub>2</sub> at high growth temperatures around 1100 °C. Under these constraints, sapphire (Al<sub>2</sub>O<sub>3</sub>) and SiC are the most popular substrate materials used currently. When hexagonal GaN is grown on the (0001) basal plane of Al<sub>2</sub>O<sub>3</sub>, a lattice misfit of ~13 % exists at the growth temperatures. A high density of threading dislocations is observed in GaN layers. The residual strain is comparable to the lattice misfit between 6H-SiC and GaN, and the result is comparable dislocation densities observed. The materials with a close lattice match with GaN, such as LiAlO<sub>2</sub> and LiGaO<sub>2</sub>, were also used for epitaxial substrates [13,14]. However, the grown GaN lacked the desired electrical properties due to either the rough growth or unintentional contamination from the substrates. The ideal candidate substrate is clearly a freestanding GaN wafer. Several research groups have been investigating the growth of the bulk GaN crystals and very thick films through various techniques such as sublimation boule-growth and hydride vapor phase epitaxy (HVPE) growth [15-18]. However, commercially available large area GaN wafers appear to be at least an away.

In addition to optical applications, GaN and related materials (especially AlGaN and AlN) are very promising candidates for demanding transistor applications such as high-power, high-frequency microwave amplifiers and switches due to their outstanding features, as stated herein. An unique feature of III-nitride materials compared to SiC is the heterostructure technology. Quantum well, modulated-doped heterointerface, and heterojunction structure can all be made in the III-nitride system. Figure 1.4 shows a typical schematic of an AlGaN/GaN heterostructure. Due to the large conduction band discontinuity, the electrons diffusing from the large bandgap AlGaN into the smaller bandgap GaN form a two-dimensional electron gas (2DEG) in the triangle quantum well at the interface. The sheet carrier density of the 2DEG is further enhanced by the strong piezoelectric effect in GaN. These piezoelectric coefficients of the III-nitride semiconductors with a Wurtzite polytype are about an order of magnitude higher than those of traditional III-V semiconductors such as GaAs and InP [19]. Theory have suggested a high peak electron velocity of

$\sim 3 \times 10^7$  cm/s and an electron mobility of  $\sim 2000$  cm<sup>2</sup>/Vs in the GaN channel at room temperature at a carrier concentration of  $10^{17}$  cm<sup>-3</sup> [20,21]. By using the 2DEG characteristics, some kinds of AlGaN/GaN high electron mobility transistors (HEMTs) have been reported. The first AlGaN/GaN modulation-doped field-effect transistors (MODFETs) were demonstrated by Khan *et al.* in 1993 [22]. These devices showed a transconductance of 23 mS/mm and 2DEG mobility of 563 cm<sup>2</sup>/Vs at 300 K. They also reported the first microwave results with a cutoff frequency  $f_T$  of 11 GHz [23]. In the early stages, the MODFETs exhibited very low transconductances and relatively poor frequency response. This is consistent with the defect-laden nature of the early GaN and AlGaN layers. With improvements in the materials quality, the transconductance, and the current capacity, a number of AlGaN/GaN heterostructure FETs (HFETs) have been reported, showing excellent device breakdown characteristics and power performance. Today, state-of-the-art AlGaN/GaN HEMTs and amplifiers exhibit an output power density larger than 20 W/mm [24]. Furthermore, an all implanted GaN junction FET (JFET), GaN metal-insulator-semiconductor FETs (MISFETs) and GaN metal-oxide-semiconductor FETs (MOSFETs) with reasonable performance have been recently reported [25-27]. These devices potentially have advantage of high-temperature operation due to low reverse leakage currents.

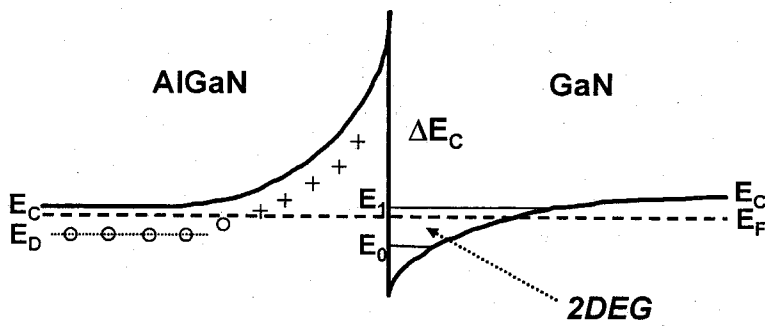


**FIG 1.4.** Conduction band structure of a modulation-doped structure.

## 1.4 Basic Technologies for GaN Power Devices

A number of GaN-based FETs with reasonable performance have already been reported, as stated herein. However, all the devices are a normally-on type. Electronic devices for EV power applications strongly require normally-off and high-temperature operation in addition to a high breakdown voltage and a large current density. At the present, any suitable devices for EV electronics have not yet been realized. Regarding GaN-based power switching devices (capable of  $300 \text{ A/cm}^2$  with 1.2 kV standoff voltage) in EV electronics, there are some possible device structures, including vertical power MOSFET, vertical JFET, and vertical MOSHFETs. In both cases, a selective-area p-type doping is considered to be a most promising processing technology to obtain normally-off operation required for EV electronics. In particular, the GaN MOSFET equipped with a surface inversion mode is important for high-power switching device applications in EV electronics, because it would provide for lower leakage currents and reduce power consumption, enabling normally-off operation with a high blocking voltage even at high temperatures. Another advantage of MOSFETs is a larger  $f_T$  over its MESFET counterpart, due to a lower capacitance between source and gate. Figure 1.5 shows a schematic of the vertical inversion-mode GaN MOSFET. In order to realize this device, we must develop some advanced processing technologies such as n- & p-type implant doping, gate insulator, freestanding GaN substrates with high conductivity, and high-temperature/high-current stable ohmic contacts. Also, there are some processing problems of etching methods of GaN for the fabrication of advanced GaN-based MOSFETs, JFETs, and/or MOSHFETs. The conventional wet etching for the GaAs technology is generally not applicable in III-nitride devices due to the high chemical stability of GaN under normal conditions. Instead, the etching of GaN has been achieved with dry etching methods, such as reactive ion-etching (RIE), or electron-cyclotron resonance (ECR) plasma etching, or inductively coupled plasma (ICP) etching. These dry etching techniques for GaN and related III-nitride materials often result in damage induced by ion bombardment. From this point of view, ion implantation doping and gate insulator are believed to become more important basic technologies for advanced GaN-based MOSFETs.

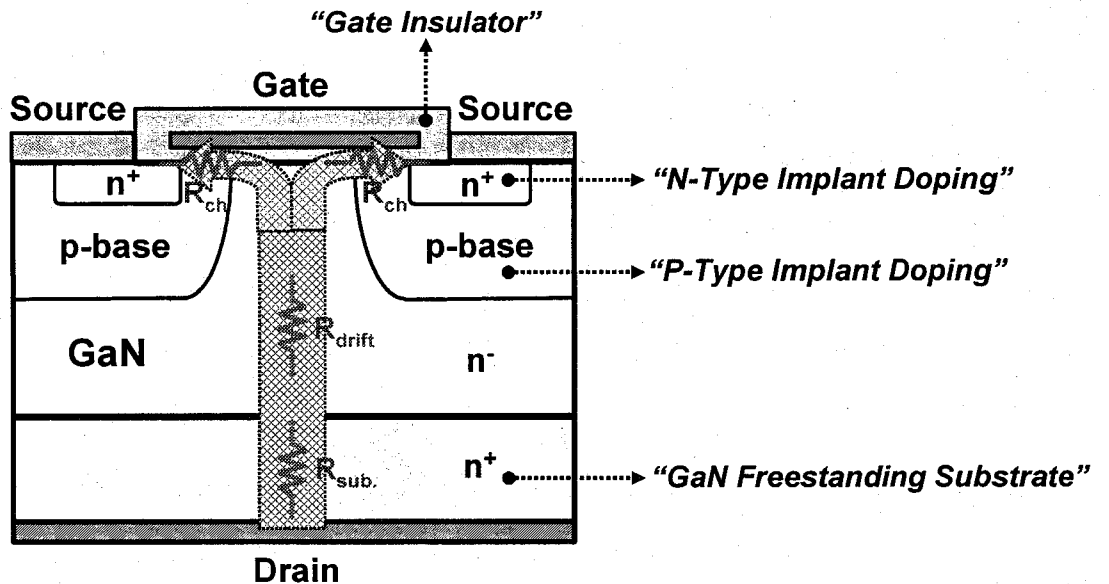


**FIG 1.5.** A schematic of vertical inversion-mode GaN MOSFET.

Ion implantation is generally an enable technology for selective-area doping or isolation of advanced electronic devices. In particular, implantation of donors at high doses can be used to decrease source and drain access resistance in FETs, at lower doses to create channel regions for FETs, while sequential implantation of both acceptors and donors may be used to fabricate pn junctions. In addition, ion implantation is a suitable technology to explore doping, compensation effects, and redistribution properties of the potential dopant species.

Furthermore, the most important requirement for GaN MOSFETs is to have a suitable gate insulator deposited or grown on GaN, which gives a low interface state density. As a consequence, the surface Fermi level must not be pinned at the insulator/GaN interface, and the charges can be accumulated or inverted, depending on the polarity of the applied voltage. Regarding gate insulators of GaN, some preliminary results are becoming available for AlN [28], SiO<sub>2</sub> [29], Si<sub>3</sub>N<sub>4</sub> [30], and Ga<sub>2</sub>O<sub>3</sub>(Gd<sub>2</sub>O<sub>3</sub>) [31]. The latter

$\text{Ga}_2\text{O}_3(\text{Gd}_2\text{O}_3)$  insulator has produced excellent characteristics on GaAs-based MOSFETs and now is applied to GaN. For all the gate insulators, the interface state densities appear well above  $10^{11} \text{ cm}^{-2}$  at the present. More studies are required to understand interfacial electrical and structural properties of various GaN MOS structures.

## 1.5 Dissertation Goal and Scope

This dissertation has focused on the development and understanding of basic technologies such as n- & p-type implantation doping and gate insulators to facilitate the fabrication of advanced inversion-mode GaN MOSFETs. The subject of this work is of interest in both the fundamental and applied fields of these basic technologies. Several important aspects of GaN processing are investigated in this work. Emphasis will be placed on achieving efficient n-type implant doping by a co-implantation technique, developing electrical characterization techniques for p-type GaN, catching sight of shallower acceptor formation by p-type implant doping, and achieving an interface state density less than  $1 \times 10^{11} \text{ eV}^{-1}\text{cm}^{-2}$  at thermally oxidized GaN MOS structures in addition to the observation of surface inversion behavior. All the work is directed towards optimizing the fabrication techniques of GaN power MOSFETs in EV electronic applications.

Chapter 2 discusses n-type implant doping of GaN, with emphasis on a co-implantation technique based on a site-competition effect. The activation processes of implanted dopants such as Ge, Si, and O using high-temperature annealing with an  $\text{SiO}_2$  capping layer are examined.

Chapter 3 presents electrical characterization of Mg-doped GaN. The dependence of deep Mg acceptors on activation annealing-temperature is revealed by using current deep-level transient spectroscopy and thermal admittance spectroscopy techniques.

Chapter 4 deals with p-type implant doping of GaN. The acceptor levels that are present in Be-implanted GaN are investigated electrically. Also, the effect of Be+O co-implantation on the Be acceptor levels is electrically examined.

In Chapter 5, GaN MOS characteristics with gate insulator such as  $\text{SiO}_2$  and/or  $\beta\text{-Ga}_2\text{O}_3$  dielectrics are

described. Additionally, gate characteristics of stacked  $\text{SiO}_2/\beta\text{-Ga}_2\text{O}_3/\text{n-GaN}$  MOS structures are also examined. Electrical properties of  $\beta\text{-Ga}_2\text{O}_3/\text{p-GaN}$  MOS diodes with  $n^+$  source regions, fabricated by thermal dry oxidation and Si+N co-implantation techniques, are also assessed.

Chapter 6 offers conclusions of the current work and an outlook for the future research.

## References

- [1] H. Morkoç, S. Strite, G. B. Gao, M.E. Lin, B. Sverdlov, and M. Burns, *J. Appl. Phys.* **76**, 1363 (1994).
- [2] T. P. Chow and R. Tyagi, *IEEE Trans. Electron Devices* **41**, 1481 (1994).
- [3] Z. Z. Bandić, P. M. Bridger, E. C. Piquette, T. C. McGill, R. P. Vaudo, V. M. Ohanse, and J. M. Redwing, *Appl. Phys. Lett.* **74**, 1266 (1998).
- [4] R. Gaska, J. W. Yang, A. Osinsky, Q. Chen, M. A. Khan, A. O. Orlov, G. L. Snider, and M. S. Shur, *Appl. Phys. Lett.* **72**, 707 (1998).
- [5] H. Amano, M. Kito, K. Hiramatsu, and I. Akasaki, *Jpn. J. Appl. Phys.* **28**, L2112 (1989).
- [6] I. Akasaki, H. Amano, M. Kito, and K. Hiramatsu, *J. Lumin.* **48/49**, 666 (1991).
- [7] S. Nakamura, T. Mukai, and M. Senoh, *Jpn. J. Appl. Phys.* **30**, L1998 (1991).
- [8] S. Nakamura, T. Mukai, and M. Senoh, *Appl. Phys. Lett.* **62**, 2390 (1993).
- [9] S. Nakamura, T. Mukai, and M. Senoh, *Appl. Phys. Lett.* **64**, 1687 (1994).
- [10] B. Goldenberg, J. D. Zook, and R. Umller, *Appl. Phys. Lett.* **62**, 381 (1993).
- [11] R. J. Molnar, R. Singh, and T. D. Moustakas, *Appl. Phys. Lett.* **66**, 268 (1995).
- [12] S. Nakamura, M. Senoh, S. Nagahama, N. Iwasa, T. Yamada, T. Matsushita, H. Kiyoku, and Y. Sugimoto, *Jpn. J. Appl. Phys.* **35**, L74 (1996).
- [13] E. S. Hellman, Z. Liliental-Weber, D. N. E. Buchanan, *MRS Internet J. Nitride Semicond. Res.* **2**, 30 (1997).
- [14] P. Kung, A. Saxler, X. Zhang, D. Walker, R. Lavado, and M. Razaghi, *Appl. Phys. Lett.* **69**, 2116 (1996).
- [15] V. A. Sukhoveyev, V. A. Ivantsov, I. P. Nikitina, A. I. Babanin, A. Y. Polyakov, A. V. Govorkov, N. B.

- Smirnov, M. G Mil'vidskii, and V. Dmitriev, MRS Internet J. Nitride Semicond. Res. **5S1**, W6.6 (2000).
- [16] A. Castaldini, A. Cavallini, L. Polenta, C. Díaz-Guerra, and J.Piqueras, J.Phys.: Condens. Matter. **14**, 13095 (2002).
- [17] W. Götz, L. T. Romano, J. Walker, N. M. Johnson, and R. J. Molnar, Appl. Phys. Lett. **72**, 1214 (1998).
- [18] C. Wetzel, D. Volm, B. K. Meyer, K. Pressel, S. Nilsson, E. N. Mokhov, and P. G. Baranov, Appl. Phys. Lett. **65**, 1033 (1994).
- [19] P. M. Asbeck, E. T. Yu, S. S. Lau, G J. Sulliran, J. M. Van Hove, and J. Redwing, Electron. Lett. **33**, 1230 (1997).
- [20] J. D. Albrecht, R. P. Wang, P. P. Ruden, M. Farahmand, and K. F. Brennan, J. Appl. Phys. **83**, 4777 (1998).
- [21] B. E. Foutz, L. F. Eastman, U. V. Bhapkar, and M. S. Shur, Appl. Phys. Lett. **70**, 2849 (1997).
- [22] M. A. Khan, A. R. Bhattarai, J. N. Kuznia, D. T. Olson, Appl. Phys. Lett. **63**, 1214 (1993).
- [23] M. A. Khan, J. N. Kuznia, D. T. Olson, W. Schatt, J. Burn, and M. S. Shur, Appl. Phys. Lett. **65**, 1121 (1994).
- [24] H. McD. Hobgood, "Silicon Carbide Crystal and Substrate Technology : A Survey of Recent Advances", Presented at 10<sup>th</sup> International Conference on Silicon Carbide and Related Materials, Proceedings, Lyon, France, 2003.
- [25] J. C. Zolper, R. J. Shul, A. G Baca, R. G Wilson, S. J. Pearton, and R. A. Stall, Appl. Phys. Lett. **68**, 2273 (1996).
- [26] S. C. Binari, Electrochem. Soc. Proc. **95-21**, 136 (1995).
- [27] F. Ren, M. Hong, S. N. G Chu, M. A. Marcus, M. J. Schurman, A. G Baca, S. J. Pearton, and C. R. Abernathy, Appl. Phys. Lett. **73**, 3893 (1999).
- [28] H. Kawai, M. Hara, F. Nakamura, and S. Imanaga, Electron Lett. **34**, 592 (1998).
- [29] H. C. Casey, Jr, G G Fountain, R. G Alley, B. P. Keller, and S. P. Denbaars, Appl. Phys. Lett. **68**, 1850 (1996).

- [30] S. Arulkumaran, T. Egawa, H. Ishikawa, T. Jimbo, and M. Umeno, *Appl. Phys. Lett.* **73**, 809 (1998).
- [31] F. Ren, M. Hong, S. N. G. Chu, M. A. Marcus, M. J. Schurman, A. Baca, S. J. Pearton, and C. R. Abernathy, *Appl. Phys. Lett.* **73**, 3893 (1998)

## Chapter 2

# N-Type Implant Doping of GaN

### 2.1 Introduction

GaN is of increasing interest for high-temperature and high-power electronic devices, as described in the previous chapter [1,2]. Various electronic devices based on GaN-related materials have already been reported [3-11]. For the design of electronic devices, particularly from a selective-area doping point of view, implantation doping offers several advantages compared to doping during film growth; the concentration of the dopants is precisely controllable in the lateral and depth distributions, and favorable elements can be implanted with sufficiently high purity. In addition, ion implantation can be widely accepted in the semiconductor industry. Recently, implantation doping of GaN has become a practical option in the design of electronic devices, with selective-area doping being of particular interest.

In general, group-IV and -II elements such as Si and Mg are promising donor and acceptor impurities for GaN, respectively. It is theoretically expected that these elements occupying a Ga-lattice site in GaN will have a low formation energy and will form donor or acceptor energy levels. As for implantation doping of GaN, several n- and p-type implantation techniques have already been reported with the use of Si [6,8,9,12-19] being the most common dopant for n-type, and Mg [8,9,12,19,20] and Ca [6,21] the main elements implanted for p-type doping. Recent studies have indicated that annealing at high temperatures is effective for high electrical activation of the implanted dopant atoms [14]. However, in the case of conventional implantation, where only one kind of dopant is used, the generation of many N vacancies and self-compensation induced by site switching may occur in the implanted region after the high-temperature annealing process. Therefore, in order to suppress the generation of N vacancies, an N-rich condition

should be created prior to implantation of the dopant atoms, and thus the implantation of additional N atoms into GaN might be expected to increase the probability of the particular dopant atoms occupying a Ga-lattice site [22,23]. In this chapter, we propose the co-implantation technique of N and dopant atoms to achieve high electrical activation of the dopant, and demonstrate that Ge+N and/or Si+N co-implantation into GaN can significantly enhance the Ge and/or Si electrical activation using Ge and Si as n-type dopants for GaN. In the previous literatures, they have not yet investigated the doping characteristics and the structural defects found in GaN when it is co-implanted and subsequently annealed. In particular, implantation-induced defects might limit the performance of the electronic devices. Therefore, the structural defects introduced by the implantation should be well understood from a viewpoint of the electronic device's applications.

Positron annihilation is an established technique for studying vacancy-type defects in semiconductors [24]. For the past few years, this technique has been used to study native defects in as-grown GaN with n- and p-type carriers [25-28], and these studies showed that positrons can be used as an effective probe for investigating vacancy-type defects and vacancy complexes in GaN. We have also studied the implantation-induced defects in GaN by means of positron annihilation, and revealed that many Ga vacancies ( $V_{Ga}$ ) are introduced by implantation. In section 2.2, we have systematically investigated the Ge-doping characteristics and structural defects of Ge+N co-implanted GaN in view of GaN stoichiometry, and the results are compared to those of conventional Ge-implanted GaN [29].

Si-doping characteristics in GaN have not yet been studied by using the co-implantation technique. As stated herein, Si is the most commonly used dopant which generates n-type conductivity in GaN. In addition, the Si implantation is expected to enhance n-type electrical activation, because Si is much lighter than Ge and consequently may introduce much less damage in GaN. In section 2.3, we have systematically investigated the Si-doping characteristics of Si+N co-implanted GaN in view of activation annealing condition, and the results are compared to those of conventional Si-implanted GaN [30].

In order to facilitate the design of the GaN MOSFET as shown in Fig. 1.4, especially from a selective-area doping point of view, implantation-doping technologies are considered as being essential. In

In particular, the combination of n- and p-type implantation-doping techniques is expected to be a powerful tool for fabricating smart electronic devices such as a power switch. However, in their doping process, high temperature annealing ( $> \sim 1200^\circ\text{C}$ ) is generally required to activate the implanted Ge and/or Si atoms, as discussed in sections 2.2 and 2.3 [29,30], whereas activation annealing should be within the temperature limits of  $1000 - 1100^\circ\text{C}$  to achieve the p-type activation [14,31,32], as stated in chapter 4. This difference of annealing temperature between n- and p-type activation may be a bottleneck when both implantation-doping techniques are simultaneously applied to the realization of their device design. In particular, thermal stability of GaN-based materials may be a concern in the high-temperature annealing process for n-type doping, since the annealing temperature is much higher than the growth temperature. Therefore, an n-type implantation-doping technique enabled relatively low-temperature activation is more desirable. Here, O is of particular interest as a possible alternative n-type dopant from the fact that O acts as a background n-type impurity in undoped GaN [21,33-36]. In addition, the O implantation doping is expected to reduce the activation annealing temperature, because O is much lighter than Ge and Si, and consequently may introduce much less damage in GaN lattice. In section 2.4, we have systematically investigated the doping characteristics of O-implanted GaN from a viewpoint of annealing temperature [37].

## 2.2 Ge+N Co-Implantation

### 2.2.1 Experimental

The GaN films used in these experiments were  $4\mu\text{m}$  thick. They were heteroepitaxially grown on a-plane sapphire substrates by atmospheric pressure metal-organic chemical-vapor deposition (MOCVD) at  $1025^\circ\text{C}$ , with a pre-deposited 20 nm GaN buffer layer grown at  $550^\circ\text{C}$ . Hydrogen was used as the main processing gas and also as the carrier gas for the metal-alkyls. Trimethylgallium (TMG) and ammonia, respectively, were used as the sources of Ga and N. The GaN films were not intentionally doped, and had a background n-type carrier concentration of  $\sim 2 \times 10^{16} \text{ cm}^{-3}$  and a mobility of  $\sim 500 \text{ cm}^2/\text{Vs}$ , as determined by room-temperature Hall-effect measurements. In order to perform electrical characterization of the as-grown

GaN films, lateral dot-and-ring Schottky diodes were fabricated as follows. Pt was evaporated as Schottky contacts, and then ohmic contacts were made by Al evaporation. The dot Pt electrode had a diameter of 500  $\mu\text{m}$ , and was surrounded by a ring Al electrode with a 1mm gap. The area of the ring electrode was 100 times greater than that of the dot electrode.

After growth, the GaN samples were implanted in a conventional ion implanter using pure  $\text{N}_2$  and  $\text{GeF}_4$  gases as the sources of the  $^{14}\text{N}^+$  and  $^{72}\text{Ge}^+$  species, respectively. First the  $\text{N}^+$  ions were implanted at energies of 35, 65, and 100 keV, respectively, to place the ion peak 53, 95, and 143 nm from the surface. The  $\text{Ge}^+$  ions were then implanted at a fixed energy of 150 keV to place its peak range at the same position as that for the  $\text{N}^+$  ions implanted at 35 keV. The N and Ge implant dosages respectively were varied between  $2 \times 10^{13}$  and  $3 \times 10^{15} \text{ cm}^{-2}$  to enable the N/Ge ratio to change. N-implanted GaN samples were also prepared for reference. All the implants were performed at nominal room temperature, with an incidence angle 7 ° away from the normal to the surface. After implantation, a 500-nm-thick  $\text{SiO}_2$  capping layer was deposited on the top surface of the samples by plasma-enhanced chemical-vapor deposition at 250 °C to provide an encapsulation cap for the subsequent implant activation annealing. All the samples were annealed on a SiC-coated graphite susceptor at 1300 °C for 5 min in flowing  $\text{H}_2$  gas at a pressure of 10 Torr. Following the anneal step, HF (49 % concentration) was used to remove the  $\text{SiO}_2$  cap, and then Al-contacts were formed at the corners of each sample by electron-beam evaporation.

The Schottky diodes fabricated on the as-grown GaN before implantation were tested by room-temperature current-voltage (*I-V*) and capacitance-voltage (*C-V*) techniques. Typical rectifier characteristics of the n-type Schottky diodes were confirmed from the *I-V* measurements. The carrier profile derived from the analysis of the *C-V* measurements was found to be uniform in the measured depth range below the surface. The average net ionized donor concentration ( $N_d - N_a$ ) at room temperature was measured to be  $\sim 2.5 \times 10^{16} \text{ cm}^{-3}$ . Characterization of deep level defects by a deep-level transient spectroscopy (DLTS) technique has also been carried out over a temperature range of 85 - 480 K, using the self-produced equipment. The steady state reverse bias and filling pulse voltages were -5 and 0 V,

respectively. The width of the filling pulse was 100  $\mu$ s, which ensured that even traps with very small electron capture cross sections were completely saturated.

The carrier activation after implantation and subsequent annealing was characterized by room-temperature Hall-effect measurements. The depth distribution of the implanted Ge atoms was measured by secondary ion mass spectrometry (SIMS). The structure of the implanted region of the GaN samples was analyzed by cross-sectional transmission electron microscopy (XTEM). Variable energy positron annihilation spectroscopy (VE-PAS) was employed at room temperature to determine the depth distribution and chemical nature of the defects in the implanted samples.

For the VE-PAS measurements, using a mono-energetic positron beam, the Doppler broadening of the electron-positron annihilation  $\gamma$ -rays ( $\sim$ 511 keV) was recorded at room temperature with a Ge detector as a function of incident positron energy  $E$ . A spectrum was measured for each value of  $E$ . The shape of the Doppler broadening spectrum was characterized by the conventional low and high electron momentum parameters  $S$  and  $W$  [38]. The momentum of an electron that a positron annihilates primarily contributes to the Doppler broadening of the resultant annihilation  $\gamma$ -rays. Therefore, the level of the Doppler broadening is a measure of the momentum state of the electron that a positron annihilates. Fundamental to this experiment is the fact that a vacancy contains only delocalized electrons, which have a low momentum, and thus annihilation in a vacancy produces a low Doppler shift. Thus high  $S$  and low  $W$  values (narrow  $\gamma$ -rays) are associated with the presence of vacancy-type defects.

## 2.2.2 Results and Discussion

Figure 2.1 shows typical DLTS spectra at various rate windows  $t_1/t_2$  measured on the fabricated Schottky diode of the as-grown GaN. The DLTS signal is the magnitude of the difference in the diode capacitance recorded at two delay times,  $t_1$  and  $t_2$ , after a filling pulse. In Fig. 2.1, the DLTS signal,  $|C(t_1) - C(t_2)|$ , is displayed for the rate windows  $t_1/t_2 = 500 \mu\text{s}/1 \text{ ms}$ ,  $4 \text{ ms}/8 \text{ ms}$ , and  $8 \text{ ms}/16 \text{ ms}$ ; the electron emission rates are 1386, 173.3, and  $86.6 \text{ s}^{-1}$ , respectively. The spectra reveal two dominant peaks at around 330 and 150 K,

which are labeled  $E_1$  and  $E_2$ . These peaks shift toward higher temperatures with an increase in the electron emission rate, which indicates that both peaks are assigned to deep-level electron traps. In the temperature range displayed in Fig. 2.1 (85 - 480 K), no other deep level could be detected with the sensitivity of  $\sim 1$  fF of our DLTS measurements.

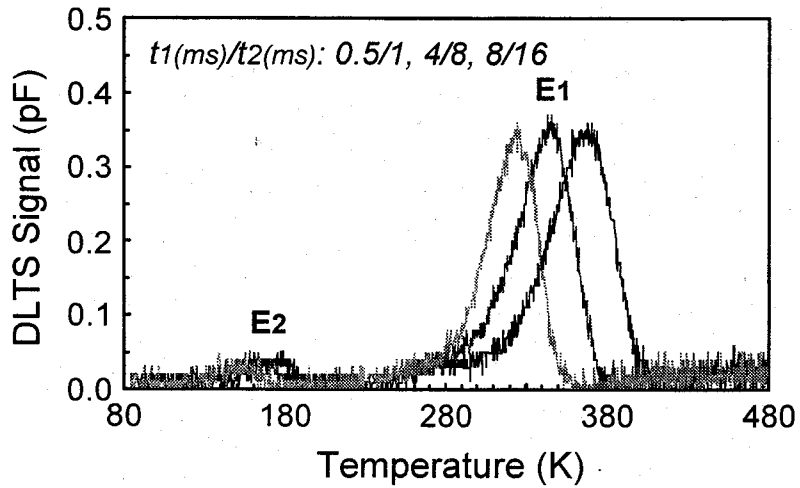


**FIG. 2.1.** DLTS spectra at various rate windows for the as-grown GaN.

The thermal activation energies for electron emission from the deep levels  $E_1$  and  $E_2$  were determined by an Arrhenius analysis of the electron emission rates. The analysis yields activation energies for electron emission into conduction band. As shown in Fig. 2.2, activation energies from the bottom of the conduction band are calculated to be  $\sim 0.59$  ( $E_1$ ) and  $\sim 0.25$  eV ( $E_2$ ) from the slope of the lines fitted to the Arrhenius plots of electron emission rates  $e_n/T^2$  for these peaks, respectively. These energies have not been corrected for any temperature dependence of the electron capture cross-section. These values are in reasonable agreement with the results previously reported in the literature [39].

The amplitude of each peak in the DLTS spectra of Fig. 2.1 relates to the concentration  $N_t$  of the

corresponding level. The  $N_i$  of the deep levels  $E_1$  and  $E_2$  are  $2.3 \times 10^{15}$  and  $3.1 \times 10^{14} \text{ cm}^{-3}$ , respectively. Their origin of these deep levels is unknown and may be native defects present in the as-grown GaN films.

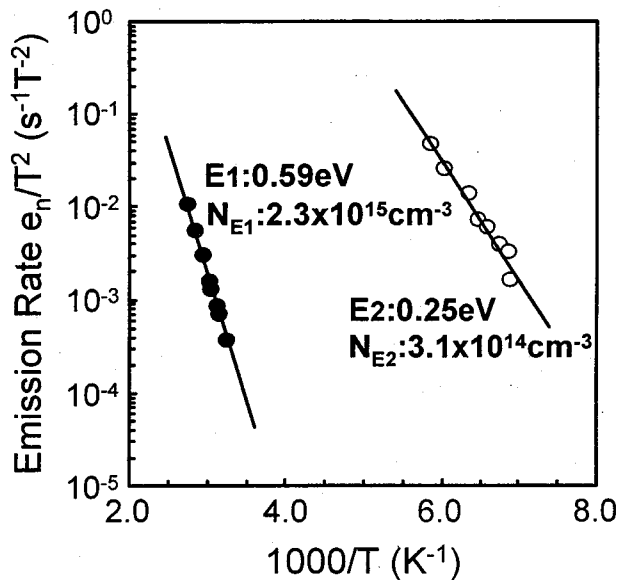


FIG 2.2. Arrhenius plots of electron emission rate  $e_n/T^2$  for the as-grown GaN.

The dependence of the depth distribution of the implanted Ge atoms on the co-implanted N peak range was investigated. The implant conditions for typical samples 1 - 4 are summarized in Table 2.1, together with their electrical data. Here, the implanted N and Ge dosages are fixed at  $1 \times 10^{15} \text{ cm}^{-2}$ . That is, an N/Ge ratio is 1 in the case of the co-implantation with N and Ge atoms. Figure 2.3 shows SIMS profiles of the implanted Ge atoms before and after annealing at  $1300^\circ\text{C}$ , together with N and Ge atomic profiles calculated by Transport of Ions in Matter software (TRIM). There is little Ge-redistribution caused by the annealing in all the SIMS profiles, regardless of the implanted N peak range. The experimental peak position of the implanted Ge atoms is in reasonable agreement with that of the TRIM calculations. This indicates that the implanted Ge atoms are stable in GaN even at very high processing temperatures. This result suggests that

long-range diffusion of the implanted Ge atoms cannot occur after annealing at 1300 °C, because of the Ge atoms being strongly bonded to the lattice. Therefore, we can say that diffusion of Ge into GaN from an external source is not practical and that ion implantation is the only possibility to introduce Ge into GaN for a selective-area doping. On the other hand, the diffusion of the implanted N atoms cannot be determined because of it being difficult to distinguish the implanted N atoms from the component N atoms of the GaN lattice even when isotope  $^{15}\text{N}$  ions were implanted.

TABLE 2.1. Implant conditions and sample characteristics

Sample	N-implant $1 \times 10^{15} \text{ cm}^{-2}$ (keV)	Ge-implant $1 \times 10^{15} \text{ cm}^{-2}$ (keV)	Sheet carrier concentration $(10^{14} \text{ cm}^{-2})$	Ge activation (%)
1	none	150	2.29	22.9 *
2	35	150	4.43	44.3
3	65	150	2.89	28.9
4	100	150	2.64	26.5

\* These data contain many carriers generated by N vacancies.

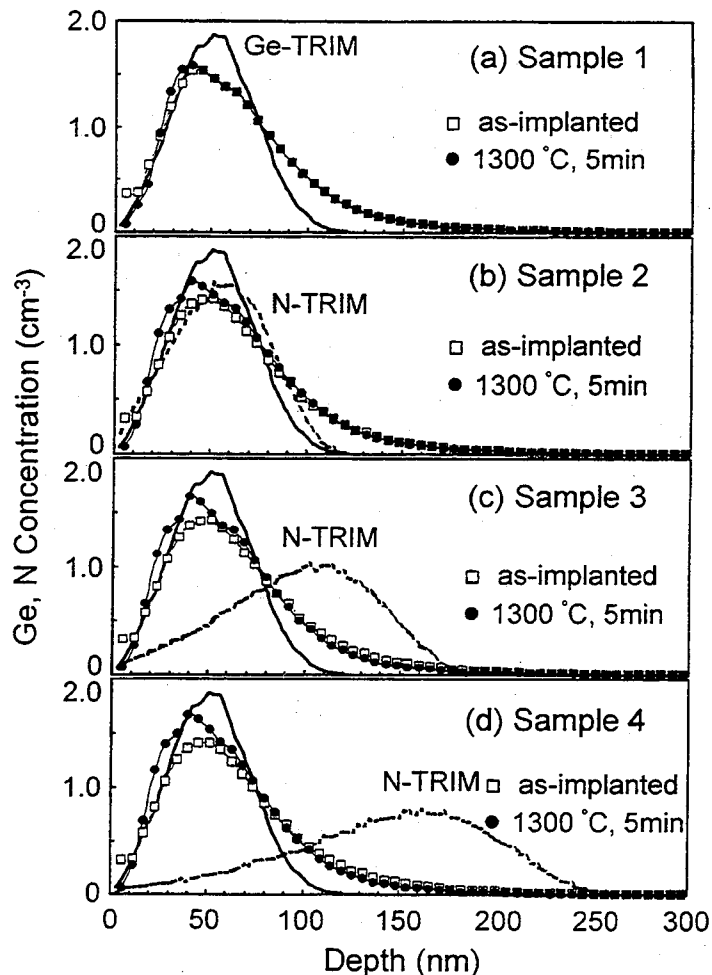


**FIG 2.3.** TRIM-simulated atomic profiles of implanted N (dashed line) and Ge (solid line) and SIMS profiles of Ge implanted in GaN, as implanted ( $\square$ ) and annealed ( $\bullet$ ) at  $1300\text{ }^{\circ}\text{C}$  for samples 1-4.

The co-implanted N peak range dependence of the Ge activation was investigated for samples 1 - 4. Assuming that the sheet carrier concentration  $n_s$  determined by Hall-effect measurements reflects the number of carriers generated from within a total region of the depth distribution of the implanted Ge atoms, effective Ge activation efficiencies ( $n_s/n_{\text{Ge}}$ ) for samples 1 - 4 can be estimated as shown in Table 2.1. Here,  $n_{\text{Ge}}$  is the Ge implant dosage. The  $n_s$  is found to strongly depend on the implanted N peak range relative to the Ge

peak one. That is, the Ge activation efficiency significantly increases with closely overlapping for the N peak range with the Ge peak one, as shown in Figs. 2.3 (b), 2.3 (c), and 2.3 (d). In particular, Ge activation efficiencies above 44 % can be achieved for sample 2, in which the N peak range is equivalently placed at the Ge peak one. On the other hand, an increase in  $n_s$  is also seen for the conventional Ge implanted sample (sample 1), which may be related to the generation of N vacancies. That is, there are insufficient N atoms to maintain the GaN stoichiometry in the Ge-implanted region. Considering that the N vacancies form a shallow donor level [40], many carriers can be generated from these N vacancies in the Ge-implanted region for sample 1. As a result, the conventional Ge implantation seems to suppress the Ge activation all the more after introducing the N vacancies. Probably, the effective Ge activation efficiency is roughly estimated to be as low as 11.5 % for sample 1, considering the increase in carrier concentration caused by the generation of many N vacancies. Therefore, the co-implantation of additional N atoms is considered to significantly enhance the Ge activation. Thus, our proposed co-implantation method with N and dopant atoms can be extremely effective in increasing electrical activation of the dopant. Furthermore, the long-range diffusion of the implanted N atoms seems not to occur after implant activation annealing from the results on the co-implanted N peak range dependence of the Ge activation.

The N/Ge ratio dependence of the Ge activation was also investigated in the Ge+N co-implantation process. Here, the dosage of the implanted Ge atoms is fixed at  $1 \times 10^{15} \text{ cm}^{-2}$ , and the implanted N peak range is also fixed (35 keV) to be equivalently placed at the Ge peak one as shown in Fig. 2.3 (b). Figure 2.4 shows room-temperature sheet carrier concentrations  $n_s$  and electron mobilities  $\mu_e$  as a function of N/Ge ratio for the Ge+N co-implanted samples after annealing at 1300 °C. The Ge activation can be classified into 3 regions in view of GaN stoichiometry; (a)  $\text{N}/\text{Ge} < 0.1$ , (b)  $0.3 < \text{N}/\text{Ge} < 3$ , and (c)  $\text{N}/\text{Ge} > 10$ . In the region (a), there are extremely insufficient N atoms available to maintain the stoichiometry of the GaN in the implanted region. Although the  $n_s$  is relatively high, the Ge activation is too poor owing to the generation of many N vacancies, as typically indicated for the conventional Ge implanted sample (sample 1). In the region (b), the  $n_s$  is kept high with a relative high  $\mu_e$  of  $\sim 50 \text{ cm}^2/\text{Vs}$  even at a Ge dosage of  $1 \times 10^{15} \text{ cm}^{-2}$ . The

Ge activation efficiencies are above 40 % under these optimum N/Ge ratio conditions. In the region (c), the  $n_s$  increases and the  $\mu_e$  significantly decreases under N-excess conditions, which may be typical characteristics of the implantation-damage caused by the increase in the total ion mass of the implanted atoms. Therefore, the optimum N/Ge ratio is found to be  $\sim 1$  for the high Ge activation.

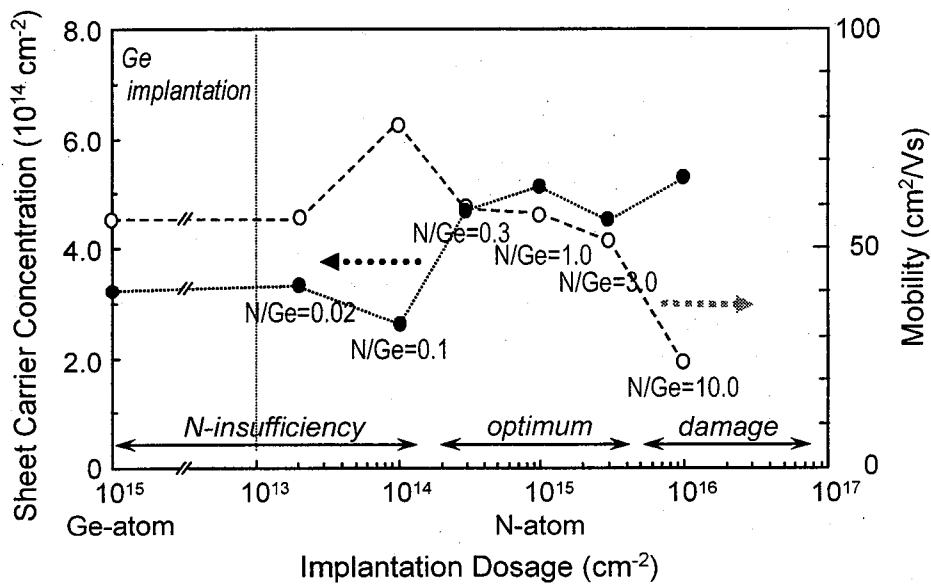


**FIG 2.4.** Dependence of sheet carrier concentration (●) and mobility (○) upon the N/Ge ratio for Ge+N co-implanted GaN samples after annealing at 1300 °C.

The Ge-doping characteristics were investigated in view of Ge implant dosage. Figure 2.5 shows the room-temperature  $n_s$  and  $\mu_e$  for the Ge+N co-implanted and subsequently annealed GaN samples as a function of Ge dosage. Here, the N implantation was performed at 35 keV to overlap the N-implanted region with the Ge one as shown in Fig. 2.3 (b), and the N/Ge ratio was fixed to be 1 for the optimum Ge activation as stated above. It is found that the  $n_s$  increases monotonically with increasing Ge implant dosage when we carried out Ge+N co-implantation, i.e. the  $n_s$  is precisely controllable between  $10^{13}$  and  $10^{15} \text{ cm}^{-2}$ .

with respect to the Ge dosage. In particular, an enhanced Ge activation level (above 40 %) can be achieved, even at a Ge dosage of  $1 \times 10^{15} \text{ cm}^{-2}$ . The  $\mu_e$  decreases gradually with increasing Ge dosage. The behavior of the  $\mu_e$  seems not to be simply consistent with the variation seen for the  $n_s$  in view of ionized impurity scattering. The  $\mu_e$  may be primarily dependent on the combined effect of ionized impurity scattering and space charge scattering induced by the presence of the implantation-introduced defects. Thus, although improved doping characteristics for Ge implantation into GaN can be successfully achieved by the Ge+N co-implantation method, the implantation-induced defects seem to remain in the implanted region even after activation annealing at  $1300^\circ\text{C}$ . In addition, the  $\mu_e$  that we observed is higher than results previously reported in the literature [12,15,20]. This indicates that Ge+N co-implantation and subsequent annealing might improve the crystallinity of the electrically activated region, which results in suppressing the space charge scattering caused by the generation of defects such as N vacancies as compared with the conventional implantation technique.

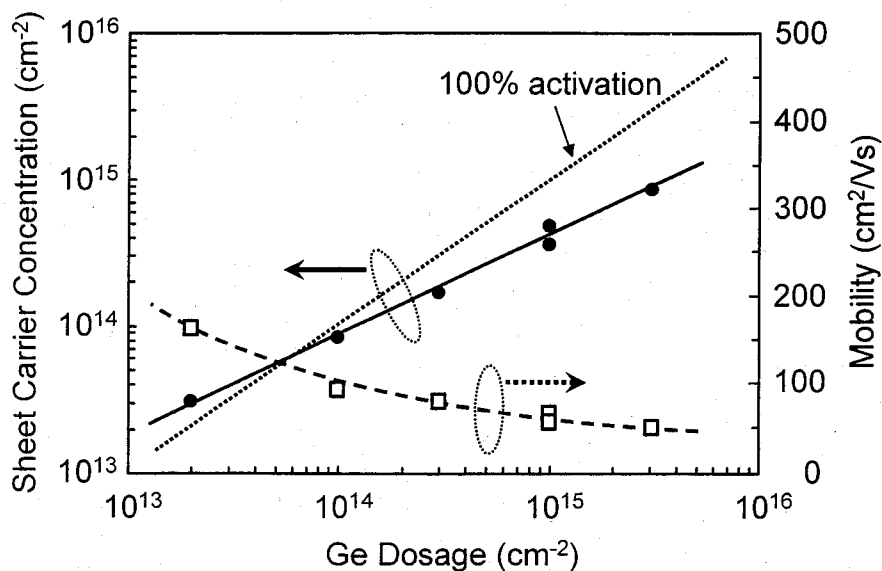


**FIG 2.5.** Sheet carrier concentration and mobility as a function of Ge implant dosage for the Ge+N co-implanted samples after annealing at  $1300^\circ\text{C}$ .

Figures 2.6 (a) and 2.6 (b) respectively show XTEM images of the Ge- (sample 1) and Ge+N- (sample 2) implanted GaN after annealing at 1300 °C. In this case, a clear difference can be seen between them. In the conventional Ge-implanted sample, a dark band exists at around ~40 nm from the surface, as shown in Fig. 2.6 (a). The position of this band is in good agreement with the distribution of the implanted Ge atoms, as determined by SIMS analysis (Fig. 2.3 (a)). Therefore this dark image is considered to correspond to the crystal damage introduced by the Ge-implantation. The width of this damaged layer was estimated to be ~15 nm. It is likely that the damage induced by implantation cannot even be removed completely by annealing at 1300 °C, because there are insufficient N atoms in the implanted region to achieve stoichiometric GaN. By contrast, no dark band can be observed in the Ge+N co-implanted GaN sample after annealing, as shown in Fig. 2.6 (b). This indicates that the damage introduced by the Ge+N co-implantation process is entirely restored by annealing at 1300 °C under N-rich conditions. Therefore, we can say that Ge+N co-implantation is significantly more effective in enabling the reconstruction of the GaN-lattice in the implanted region, resulting in an improvement in the crystallinity of the electrically activated region. In addition, the implantation-induced defects cannot be observed for the N-implanted sample after annealing, as shown in Fig. 2.6 (c). From this result, the co-implantation of additional N atoms into GaN might be expected to introduce much less damage in the implanted region than the implantation of Ge dopant atoms.

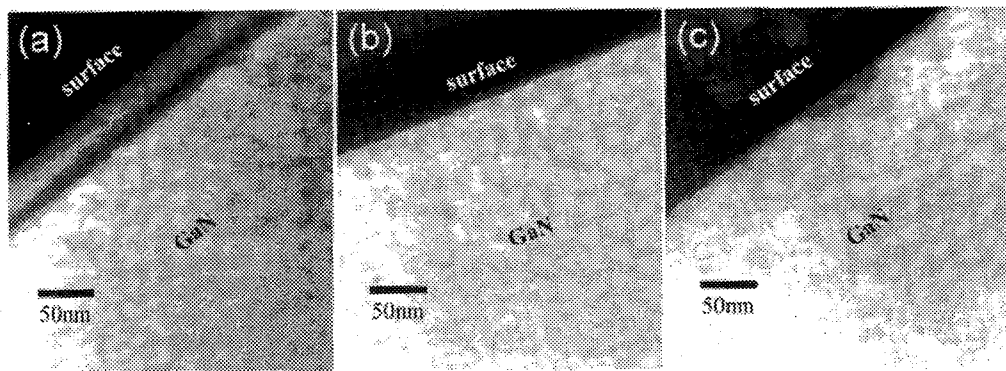


**FIG 2.6.** XTEM micrographs of Ge-, Ge+N-, and N-implanted GaN samples with a dosage of  $1 \times 10^{15} \text{ cm}^{-2}$  after annealing at 1300 °C.

Figure 2.7 shows the  $S$  parameter as a function of  $E$  for the Ge- (sample 1) and Ge+N- (sample 2) implanted GaN before annealing, respectively. The results of an as-grown GaN epitaxial layer and a sample implanted with N at 35 keV are also shown. In this case, the N and Ge dosages are fixed at  $1 \times 10^{15} \text{ cm}^{-2}$ . For the as-grown GaN before implantation, when positrons are implanted close to the surface with  $E = 0 - 1$  keV, the  $S$  parameter is nearly 0.445, which characterizes the defects and chemical nature of the near-surface region (0 - 5 nm) of the sample. At  $E$  of 5 - 50 keV, depending on the thickness of the GaN layer, the  $S$  parameter is almost constant, which indicates that all positrons annihilate in the GaN layer. The data measured at these energies can be taken as characteristics of the GaN layer, which have been reported to be attributed to a negatively charged Ga-vacancy ( $V_{Ga}$ ) of native point defects in the GaN lattice [25,26]. At  $E > 50$  keV, the  $S$  parameter decreases as the annihilation starts to occur at the sapphire substrate. For the as-implanted GaN before annealing, the  $S$  parameter at  $E < 50$  keV reflecting the characteristics of the GaN layer increases largely as compared with that of the as-grown sample. This increased  $S$  parameter indicates that the positron-electron momentum distribution is narrower than in the as-grown sample. This narrowing is due to positron annihilating as trapped at vacancy-type defects, where the electron density is lower and the probability of annihilation with high-momentum core electrons is reduced. Thus, this increase in  $S$  parameter is a clear sign of vacancy-type defects introduced by the ion implantation. This increased  $S$  value is also found to depend on the total ion mass of the implanted atoms. That is, the  $S$  parameter increases with increasing the total ion mass, indicating that these  $S$  values are probably associated with the concentrations of the vacancy-type defects introduced by the implantation, as discussed later. In addition, the  $S$  parameter decreases gradually with increasing  $E$  for all the as-implanted samples. This indicates that part of the defects introduced in the implanted region diffuses into the deeper-lying region of the GaN layer during the implantation. This long-range diffusion of the defects may be related to dislocations characteristic of the heteroepitaxial GaN, caused by the lattice-mismatch between the GaN layer and the sapphire substrate (Fig. 2.8).

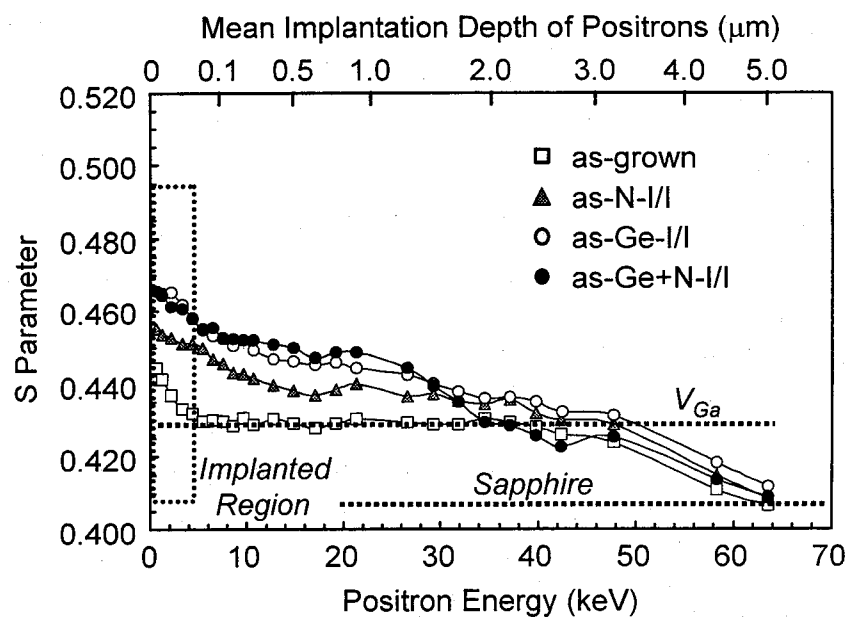


**FIG 2.7.** S parameter as a function of incident positron energy for N-, Ge-, and Ge+N-implanted GaN samples with a dosage of  $1 \times 10^{15} \text{ cm}^{-2}$  before annealing at  $1300^\circ\text{C}$ .

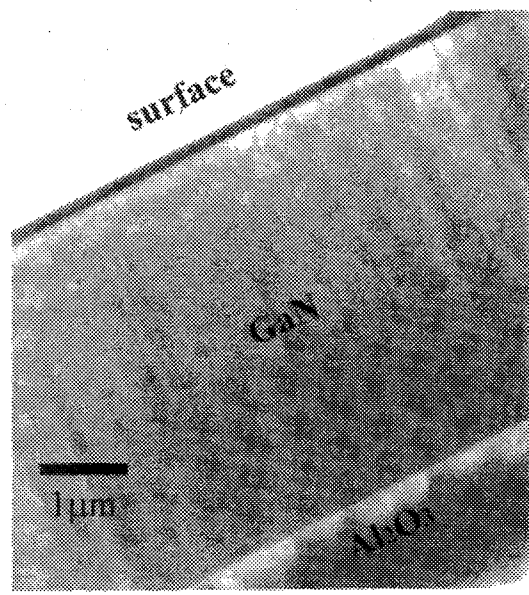


**FIG 2.8.** XTEM micrographs of as-grown GaN.

Figure 2.9 shows the  $S$  and  $W$  parameters as a function of  $E$  for the N-, Ge- (sample 1) and Ge+N- (sample 2) implanted GaN after annealing at 1300 °C, respectively. The results of the as-grown GaN epitaxial layer are also shown as a reference. As for the annealed samples, a marked difference in VE-PAS spectra can be seen between the N-implanted sample and the implanted samples with the use of Ge. A striking peak with a much higher  $S$  value of ~0.500 and a much lower  $W$  value of ~0.073 is detected at  $E$  of 0 - 4 keV for both the Ge- and Ge+N-implanted samples. This indicates that the positron-electron

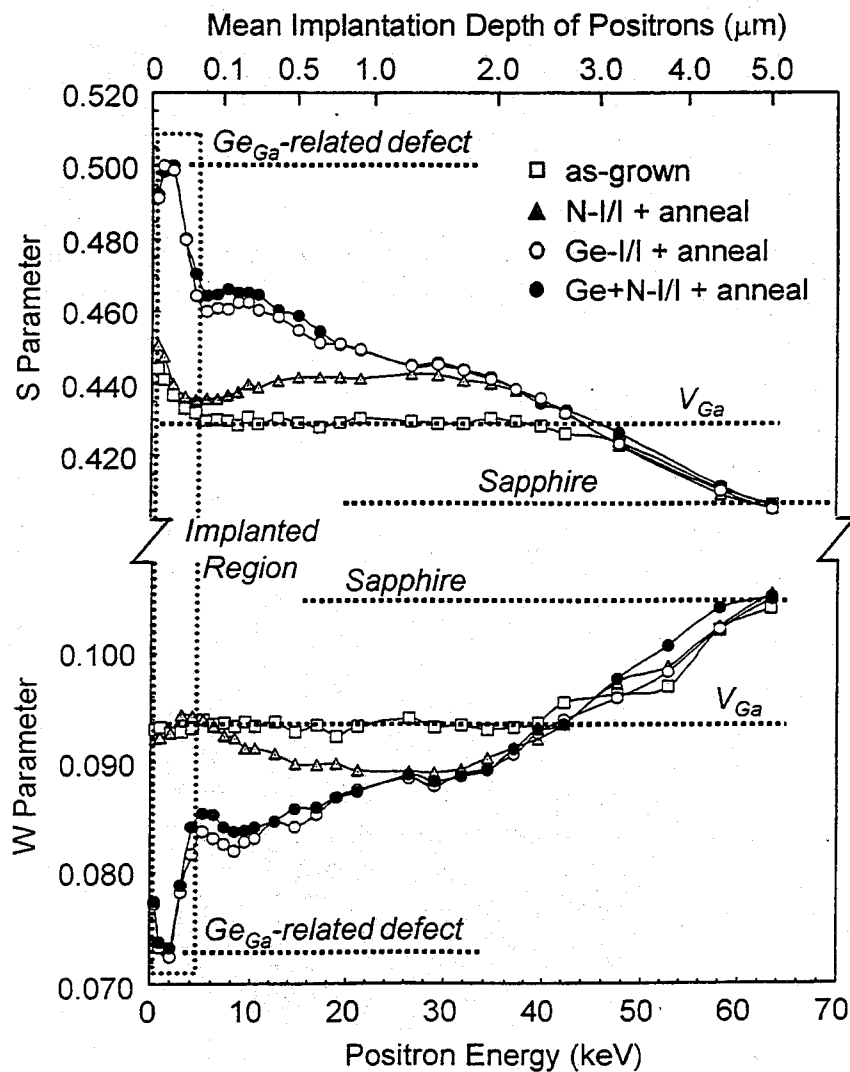


**FIG. 2.9.**  $S$  and  $W$  parameters as a function of incident positron energy for N-, Ge-, and Ge+N-implanted GaN samples with a dosage of  $1 \times 10^{15} \text{ cm}^{-2}$  after annealing at 1300 °C.

momentum distribution is much narrower in this depth range. Probably, the narrowing is due to positrons annihilating as trapped at new vacancy-type defects, which are obviously different from those of the as-grown and as-implanted samples. For the N-implanted sample, however, this peak cannot be observed. Considering that the depth range corresponding to the 0 - 4 keV range is in good agreement with the region of the implanted Ge atoms from the SIMS profiles, this striking peak is probably associated with the electrical activation and/or the implanted Ge atoms. In addition, at  $E$  of 10 - 40 keV reflecting the characteristics of the GaN layer, the increase in  $S$  parameter and the decrease in  $W$  parameter can be seen for all the annealed samples, respectively, compared with those of the as-implanted samples. This result suggests that the annealing may induce the increase in size of the implantation-introduced defects rather than the increase in concentration of them.

The number of different vacancy-type defects trapping positrons can be investigated through the linearity between the  $S$  and  $W$  parameters [25,26,41]. If only a single type of vacancy is present, the  $W$  parameter depends linearly on the  $S$  parameter. As for all the samples, the  $S$  and  $W$  parameters at  $E$  of 0 - 30 keV are plotted in Fig. 2.10. It is found that all the data of the as-implanted samples fall on the same straight line (—). This indicates that the same vacancy-type defect is present in all the as-implanted samples, regardless of the species of the implanted atoms such as N, Ge, and Ge+N. Thus, the different  $S$  parameters of the as-implanted samples as shown in Fig. 2.7 reflect the variation in concentration of the vacancy-type defects introduced by the implantation. From the slope of the dotted line of the as-implanted samples as shown in Fig. 2.10, the characteristic  $\Delta W/\Delta S$  ratio of  $\sim 0.225$  can be calculated, which value is the same one of the as-grown GaN reference sample. This suggests that the implantation-induced defects in all the as-implanted samples can be identified as the same kind of  $V_{Ga}$  defects detected for the as-grown GaN sample. On the other hand, as for the annealed samples, all the data at  $E$  of 10 - 30 keV also fall on the same straight line (—), which is different from that of the as-implanted samples. In this case, the characteristic  $\Delta W/\Delta S$  ratio is  $\sim 0.284$ , which is a little higher than that of the as-implanted samples. Thus, the same vacancy-type defects must be present in all the annealed samples, which are different from the  $V_{Ga}$  defects for the as-grown and

as-implanted samples. These results suggest that the implantation-introduced  $V_{Ga}$  defects change into  $V_{Ga}$ -related defects with different character by the annealing at 13000 °C. As stated above, the newly observed  $V_{Ga}$ -related defects for the annealed samples are expected to have larger open volume than that of the  $V_{Ga}$  in the as-grown and as-implanted samples, such as a divacancy, a vacancy-cluster and a vacancy-impurity complex [42] etc. Moreover, for both the Ge- and Ge+N-implanted samples after annealing, the data at  $E$  of 0 - 4 keV deviate extremely from the solid line of the annealed samples, which behavior is obviously different from that of the N-implanted sample after annealing. This characteristic  $\Delta W/\Delta S$  ratio is calculated to be ~0.353, which is much higher than those of the as-implanted and annealed samples. Considering that the depth range corresponding to the 0 - 4 keV range is consistent with the electrically activated regions as mentioned above, this significant increase in  $\Delta W/\Delta S$  ratio is probably associated with the implanted Ge dopant-atoms occupying a Ga-lattice site in GaN. In other words, Ge-related vacancy-type defects with marked different character are considered to be newly created by the implant activation annealing at 1300 °C for both the Ge- and Ge+N-implanted samples.

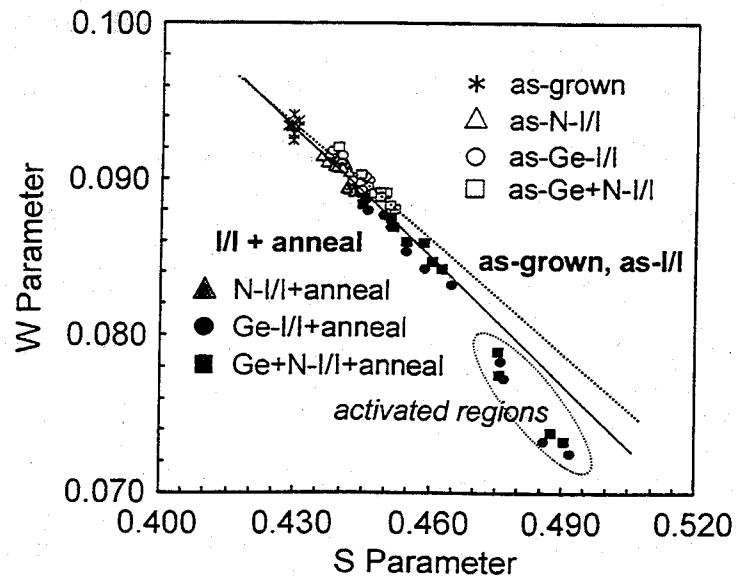


**FIG 2.10.** S parameter versus W parameter for N-, Ge-, and Ge+N-implanted GaN samples with a dosage of  $1 \times 10^{15} \text{ cm}^{-2}$  before and after annealing at 1300 °C.

In summary, we have demonstrated that co-implantation with N and Ge atoms into GaN markedly enhances the Ge electrical activation based on the site-competition effect. In particular, overlapping of the N-implanted region with the Ge one makes the Ge activation higher. The Ge+N co-implantation can achieve Ge activation efficiencies higher than 40 % at the optimum N/Ge ratio of ~1, whereas the conventional Ge implantation seems to suppress the Ge activation owing to the generation of N vacancies. TEM observations reveal that the implantation-induced damage is entirely restored by activation annealing for the Ge+N co-implantation, in contrast to the case of the conventional Ge implantation process. However, VE-PAS measurements revealed that markedly different vacancy-type defects are created in the electrically activated regions by annealing in both Ge- and Ge+N-implanted samples.

## 2.3 Si+N Co-Implantation

### 2.3.1 Experimental

The epitaxial GaN films used in these experiments were 1  $\mu\text{m}$  thick. They were grown on a-plane sapphire substrates by atmospheric pressure MOCVD at 1050 °C, on a pre-deposited 20 nm AlN buffer layer grown at 400 °C. The GaN films were not intentionally doped, and showed semi-insulating properties. After growth, the GaN samples were implanted using pure  $\text{N}_2$  and  $\text{SiF}_4$  gases as the sources of the  $^{14}\text{N}^+$  and  $^{28}\text{Si}^+$  species, respectively. First the  $\text{N}^+$  ions were implanted at energies of 35, 65, and 100 keV, respectively, to position the ion peak 53, 95, and 143 nm from the surface. The  $\text{Si}^+$  ions were then implanted at a fixed energy of 65 keV to place its peak range at the same position as that for the  $\text{N}^+$  implanted at 35 keV. The N and Si implant dosages were varied between  $1 \times 10^{13}$  and  $1 \times 10^{16} \text{ cm}^{-2}$ . In the case of the Si+N co-implantation, the N/Si ratio was kept ~1 for an optimum doping, as reported in section 2.2. Conventional Si- and N-implanted GaN samples were also prepared for reference. All the implants were performed at room temperature, with an incidence angle 7° off the normal surface. After implantation, a 500-nm-thick  $\text{SiO}_2$  capping layer was deposited on the top surface of the samples by radio-frequency sputtering at room temperature to provide an encapsulation cap for the subsequent implant activation annealing. All the

samples were annealed on a SiC-coated graphite susceptor at temperatures between 1100 and 1300 °C in flowing H<sub>2</sub> gas at a pressure of 10 Torr. Following the anneal step, HF (49 % concentration) was used to remove the SiO<sub>2</sub> cap, and then Al-contacts were formed at the corners of each sample by electron-beam evaporation. Carrier activation was characterized by room-temperature Hall-effect measurements. Hall data of sheet carrier concentration  $n_s$  and electron mobility  $\mu_e$  were in error by less than 1 % on these measurements. The depth distribution of the implanted Si atoms was measured by SIMS. The surface morphology of the implanted region of the GaN samples was analyzed by atomic force microscopy (AFM). Annealing behavior of defects introduced by Si implantation was assessed by means of VE-PAS measurements, using a mono-energetic positron beam.

### 2.3.2 Results and Discussion

The dependence of the depth distribution of the implanted Si atoms on the co-implanted N peak range was investigated. The implant conditions for typical samples, numbered 1 - 4, are summarized in Table 2.2, together with their electrical data. Here, the implanted N and Si dosages were fixed at  $1 \times 10^{15} \text{ cm}^{-2}$ . Figure 2.11 shows SIMS profiles of the implanted Si atoms before and after annealing at 1300 °C for 5 min, together with N and Si atomic profiles calculated by TRIM. Before the annealing, the experimental peak position of the implanted Si atoms is in reasonable agreement with that of the TRIM calculations, regardless of the implanted N peak range. Furthermore, the implanted Si atoms are found to diffuse into a little deeper-lying region of the GaN films by the annealing at 1300 °C, which seems to be also independent on the N implant conditions. This annealing-induced diffusion is different from the situation of Ge+N co-implantation, as reported in section 2.2. That is, this redistribution of the implanted Si atoms may occur due to Si having much lighter ion mass than Ge. In addition, Si atoms cannot be detected for N-implanted GaN after the annealing by the SIMS measurements. This suggests that the diffusion of Si atoms into GaN from an SiO<sub>2</sub> encapsulation layer cannot occur during the high-temperature annealing process and consequently that the use of the SiO<sub>2</sub> cap does not influence the Si-doping characteristics, as discussed later. On the other hand,

the diffusion of the implanted N atoms cannot be determined because of it being difficult to distinguish the implanted N atoms from the component N atoms of the GaN lattice even when isotope  $^{15}\text{N}$  atoms were implanted.

**TABLE 2.2** Implant conditions and sample characteristics

Sample	N-implant $1\times 10^{15} \text{ cm}^{-2}$ (keV)	Si-implant $1\times 10^{15} \text{ cm}^{-2}$ (keV)	Sheet carrier concentration ( $10^{14} \text{ cm}^{-2}$ )	Mobility ( $\text{cm}^2/\text{V}\cdot\text{s}$ )
1	none	65	5.85	80.2
2	35	65	4.87	98.5
3	65	65	5.27	86.8
4	100	65	6.84	75.8

The co-implanted N peak range dependence of the Si activation was investigated for typical samples 1 - 4. Here, the activation annealing was performed at 1300 °C for 5 min. First, a difference of electrical properties is found between the conventional Si-implanted samples (sample 1) and the Si+N co-implanted sample (sample 2), as shown in Table 2.2. Sample 2 shows a lower  $n_s$  and a higher  $\mu_e$  than sample 1, in spite of the identical Si dosage of  $1\times 10^{15} \text{ cm}^{-2}$  for both samples. In particular, the high  $\mu_e$  of  $\sim 100 \text{ cm}^2/\text{Vs}$  can be achieved even at a Si dosage of  $1\times 10^{15} \text{ cm}^{-2}$  for the co-implanted sample 2 in which the N peak range is equivalently placed at the Si peak one. This reflects high quality of the GaN lattice in the co-implanted region compared to the conventional Si-implanted one. Si activation efficiency of sample 2 is estimated to be  $\sim 49\%$  from the implanted Si dosage of  $1\times 10^{15} \text{ cm}^{-2}$ . As compared to sample 2, the high  $n_s$  seen for sample 1 may be related to the generation of N vacancies besides the Si electrical activation. That is, there are extremely insufficient N atoms available to maintain GaN stoichiometry in the conventional Si-implanted region. Considering that the N vacancies ( $V_N$ ) form a shallow donor level [40], many carriers can be

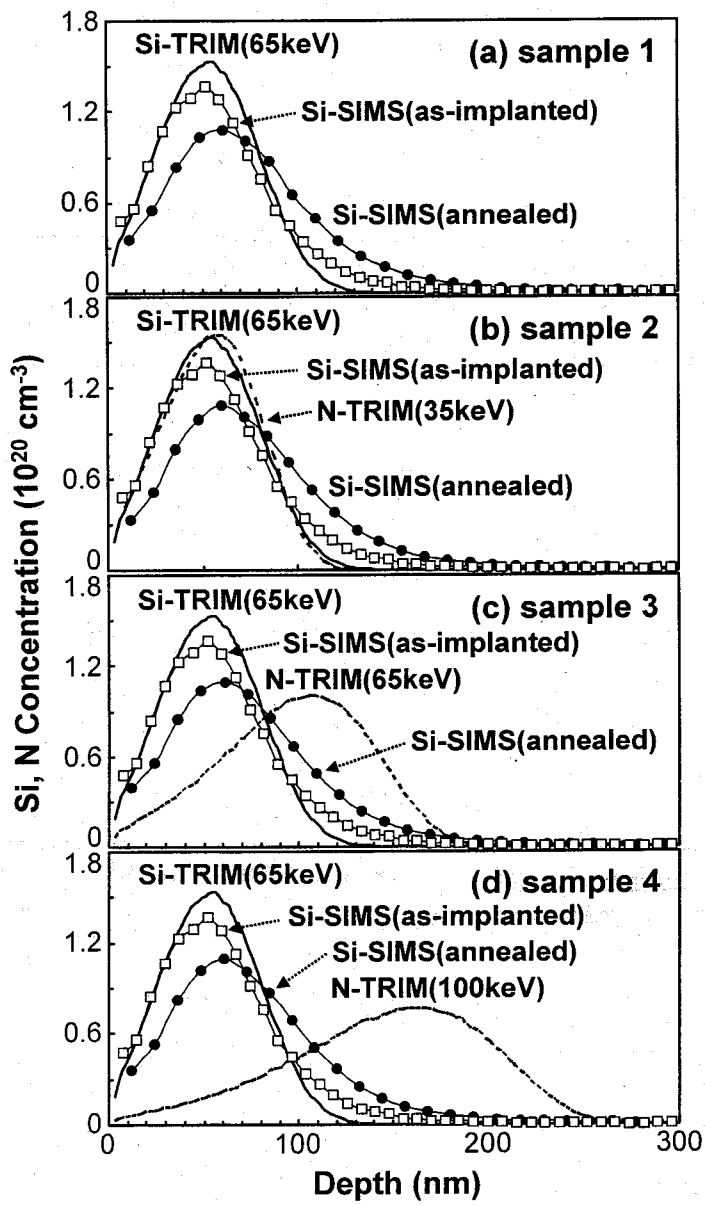


**FIG 2.11.** TRIM-simulated atomic profiles of implanted N (dashed line) and Si (solid line) and SIMS profiles of Si implanted in GaN, as implanted ( $\square$ ) and annealed ( $\bullet$ ) at  $1300^\circ\text{C}$  for samples 1-4.

generated from these  $V_N$ . As a result, the conventional Si implantation may show an increase in  $n_s$  all the more after introducing the N vacancies. In this case, the concentration of the N vacancies generated should be ideally equal to that of the implanted Si atoms. That is, the effective carriers from the Si doping except for the N vacancies may be assumed to be only half the  $n_s$ . Thus, the actual Si activation efficiency is roughly estimated to be as low as 29 % for sample 1, considering the increase in carrier concentration caused by the generation of many N vacancies. On the other hand, in the case of the Si+N co-implanted GaN samples (samples 2 - 4), the  $n_s$  and  $\mu_e$  strongly depend on the implanted N peak range relative to the Si peak one, as shown in Table 2.2. The  $n_s$  decreases and the  $\mu_e$  increases with closely overlapping for the N peak range with the Si peak one. From our previous study of the Ge+N co-implantation [29], as reported in section 2.2, the distribution of the co-implanted N atoms is expected to be unchanged even after the annealing at 1300 °C. In addition, the N-implanted GaN sample shows semi-insulating properties after the annealing. Thus, the observed increase in  $n_s$  is considered to be caused by the combined effects of Si-doping and N-vacancy generation for the co-implanted samples (samples 3 and 4) in which the N peak range does not completely overlap with the Si peak one. Therefore, we can say that the co-implantation of additional N atoms significantly enhances the actual Si electrical activation when the N peak range is equivalently placed at the Si peak one.

Here, these results on the Si+N co-implantation are compared with our previous study on the Ge+N one. The  $n_s$  and  $\mu_e$  obtained for the Ge+N system are lower than those for the Si+N system, under the same condition where the N peak range overlapped with the dopant peak range. In particular, the Ge+N co-implanted GaN samples show much lower  $\mu_e$  of 50 - 60 cm<sup>2</sup>/Vs. In addition, the N peak range dependence of  $n_s$  seen for the Ge+N system is found to be just the opposite of that for the Si+N system. That is, the  $n_s$  increases with relatively low  $\mu_e$  with closely overlapping for the N peak range with the Ge peak one for the Ge+N co-implanted GaN samples. These differences that we observed are considered to be caused by a considerable margin of ion mass between Si and Ge; the Ge+N co-implantation process should be inclusive of implantation-induced damage in addition to the combined effects of the Ge-doping and the

N-vacancy generation. Conversely, the Si+N co-implantation may suppress the damage due to Si being much lighter than Ge, as expected. Therefore, we can say right enough that the Si+N co-implantation technique is a more effective method for achieving high quality n-type doped GaN by implantation, based on an ideal site-competition effect.

The annealing-condition dependence of the Si activation was also investigated in the Si+N co-implantation process. The implant condition was the same one as sample 2 in which the implanted N peak range overlaps with the Si peak one, as shown in Table 2.2. Figure 2.12 (a) shows room-temperature  $n_s$  and  $\mu_e$  as a function of annealing temperature for the Si+N co-implanted samples. Here, annealing time was fixed at 5 min. With the rising of annealing temperature from 1100 to 1200 °C, the  $n_s$  significantly increases from  $2 \times 10^{12} \text{ cm}^{-2}$  to  $3 \times 10^{14} \text{ cm}^{-2}$  with high  $\mu_e$  of  $\sim 75 \text{ cm}^2/\text{Vs}$ . This indicates that the Si electrical activation starts to occur at around 1200 °C. On the other hand, the  $\mu_e$  significantly increases in spite of the  $n_s$  being saturated by the annealing at 1300 °C. This behavior indicates an improvement in the crystallinity in the electrically activated region. Therefore, the annealing at high temperatures above 1200 °C is required to activate the implanted Si atoms in GaN. Figure 2.12 (b) shows room-temperature  $n_s$  and  $\mu_e$  as a function of annealing time at 1300 °C for the Si+N co-implanted samples. The  $n_s$  gradually increases with an increase of annealing time, whereas the  $\mu_e$  significantly increases from  $51 \text{ cm}^2/\text{Vs}$  to  $103 \text{ cm}^2/\text{Vs}$ . This result also suggests a significant improvement of the crystallinity under an optimum condition of GaN stoichiometry in accordance with increasing annealing time.

Moreover, Si-doping characteristics were investigated in view of Si implant dosage. Figure 2.13 shows the room-temperature  $n_s$  and  $\mu_e$  as a function of Si dosage for the Si+N co-implanted and subsequently annealed GaN samples. Here, the N implantation was performed at 35 keV to overlap the N-implanted region with the Si one as shown in Fig. 2.11 (b), and the N/Si ratio was fixed at 1 for the optimum Si activation as stated above. The activation annealing was carried out at 1300 °C for 5 min. The  $n_s$  increases monotonically with increasing Si implant dosage up to  $1 \times 10^{15} \text{ cm}^{-2}$  under the Si+N co-implantation process, that is, the  $n_s$  seems to be precisely controllable between  $3 \times 10^{12}$  and  $5 \times 10^{14} \text{ cm}^{-2}$  with respect to the Si dosage.

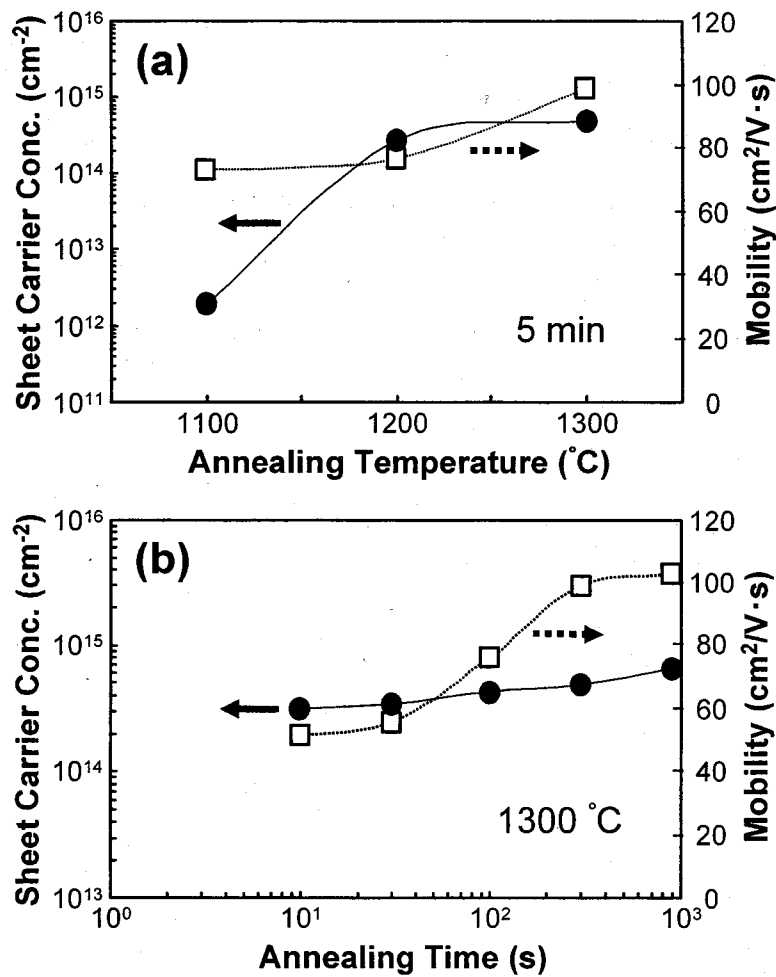


**FIG 2.12.** Sheet carrier concentration (●) and mobility (□) as a function of (a) annealing temperature and (b) annealing time for Si+N co-implanted GaN samples with Si and N dosages of  $1 \times 10^{15} \text{ cm}^{-2}$ .

An enhanced Si activation level of ~50 % is attained in this region of the Si dosage. Therefore, improved doping characteristics for Si implantation into GaN can be successfully achieved by the Si+N co-implantation method. On the other hand, the  $\mu_e$  decreases gradually with increasing Si dosage in this region. However, the behavior of the  $\mu_e$  seems not to be simply consistent with the variation seen for the  $n_s$  in view of ionized

impurity scattering. The  $\mu_e$  may be primarily dependent on the combined effect of ionized impurity scattering and space charge scattering induced by the presence of the implantation-introduced defects. In addition, the observed  $\mu_e$  is much higher than results previously reported in the literature [12,15,20,29]. This indicates that the Si+N co-implantation and subsequent annealing might significantly improve the crystallinity of the electrically activated region, which results in suppressing the space charge scattering caused by the generation of defects such as N vacancies, as compared with the conventional implantation technique. Furthermore, the  $n_s$  and  $\mu_e$  seem to be saturated at around  $1 \times 10^{15} \text{ cm}^{-2}$  and  $71 \text{ cm}^2/\text{Vs}$ , respectively, with increasing the Si dosage above  $3 \times 10^{15} \text{ cm}^{-2}$ . This result suggests that the Si-doping characteristics by the implantation technique may attain to the solid-solubility limit of the implanted Si atoms into GaN. This phenomenon is probably associated with the amorphous-phase transformation of GaN formed by high-dose ion-implantation.

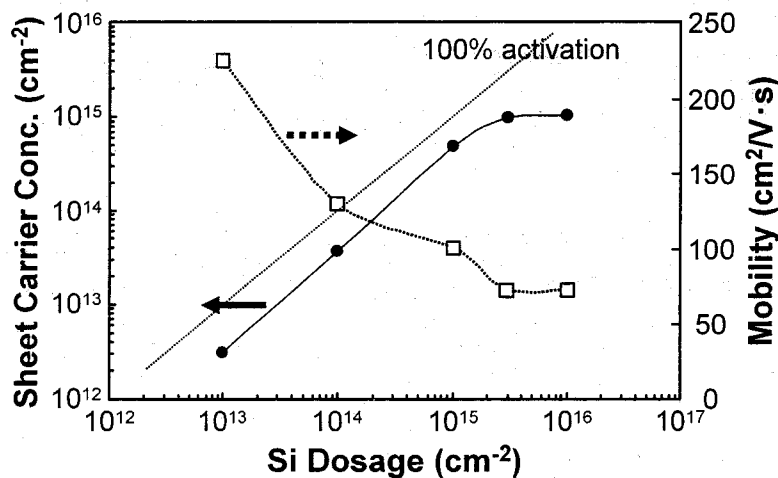


**FIG 2.13.** Sheet carrier concentration (●) and mobility (□) as a function of Si implant dosage for the Si+N co-implanted samples after annealing at 1300 °C.

In this study, improved Si-doping characteristics have been achieved for GaN by the Si+N co-implantation where the N/Si ratio was fixed at 1. However, there seem to be numerous implantation-induced damage and N vacancies even after the high temperature annealing process. Thus, the N/Si ratio needs to be optimized to attain a more improvement in Si-doping characteristics and crystallinity of the co-implanted GaN.

Figures 2.14 (a) and 2.14 (b), respectively, show typical AFM images of the Si- (sample 1) and Si+N- (sample 2) implanted GaN after annealing at 1300 °C for 5 min. A clear difference can be seen between them. In the co-implanted GaN sample, a number of growth steps are clearly observed as shown in Fig. 2.14 (b), which surface morphology is identical with that of the as-grown GaN before implantation. That is, the surface morphology is found to be unchanged even after the implantation and subsequent annealing processes for the co-implanted GaN. Here, the dark points correspond to threading dislocations. In sharp contrast, many white-colored islands with ~25 nm in height and ~140 nm in diameter can be seen for the conventional Si-implanted sample, as shown in Fig. 2.14 (a). These islands were found to be mainly composed of Ga from Auger electron spectroscopy (AES) measurements. These Ga islands in surface

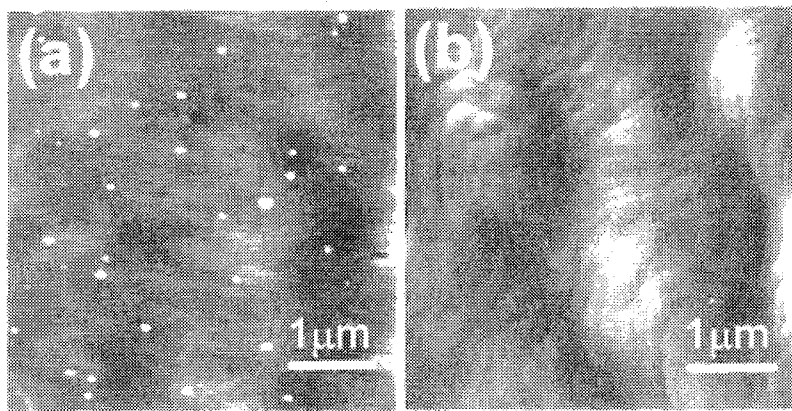


**FIG 2.14.** AFM images of Si- and Si+N-implanted GaN samples with a Si dosage of  $1 \times 10^{15} \text{ cm}^{-2}$  after annealing at 1300 °C. Both images are  $5 \times 5 \mu\text{m}^2$ .

region are considered to be formed in accordance with GaN dissociation caused by the high-temperature annealing. In particular, in the case of the conventional Si implantation, the Ga islands are expected to be more easily formed owing to there being insufficient N atoms in the implanted region to achieve stoichiometric GaN as compared to the Si+N co-implantation process. In addition, the growth steps are not clearly seen for the Si-implanted sample, which is in reasonable agreement with the GaN dissociation in the surface region. Thus, the Si+N co-implantation turns out to be significantly suppressed the Ga-island formation in view of GaN stoichiometry. Therefore, we can say that the co-implantation technique is more effective in enabling the reconstruction of the GaN-lattice in the implanted surface region, resulting in an improvement in the crystallinity of the electrically activated region. However, implantation-induced micro-defects “small holes” can be seen even after the high-temperature annealing process for both Si- and Si+N-implanted samples, as shown in Figs. 2.14 (a) and 2.14 (b). For reference, the micro-defects cannot be observed for the N-implanted sample after annealing, indicating that the co-implantation of additional N atoms into GaN might be expected to introduce much less damage in the implanted region than the implantation of Si dopant atoms. In addition, the micro-defects observed in both the Si- and Si+N-implanted GaN are probably associated with the implantation of Si atoms and may have some kind of relation to the defects characteristic of both the Ge- and Ge+N-implanted GaN as determined by VE-PAS measurements, as reported in section 2.2.

In order to clarify the annealing behavior of the defects introduced by Si implantation, VE-PAS measurements, using a mono-energetic positron beam, have been applied to Si-implanted GaN samples before and after annealing at various temperatures between 100 and 1300 °C [43]. Here, the  $\text{Si}^+$  ions were implanted into undoped GaN at 65 keV with a dosage of  $8.5 \times 10^{14} \text{ cm}^{-2}$ . Figure 2.15 shows a SIMS profile of the implanted Si atoms before annealing, together with a Si atomic profile calculated by TRIM. The experimental peak position ( $R_p$ ) of the Si atoms is located at ~50 nm from the surface, which is in reasonable agreement with that of the TRIM calculation. Also, the peak concentration of the Si atoms is about  $1 \times 10^{20} \text{ cm}^{-3}$ . In the deeper lying region than the  $R_p$ , however, the experimental concentration of the Si atoms is

apparently much higher than the calculated one. This observed tailing of the Si atoms, largely deviated from the TRIM simulation, may be caused by a channeling effect even with an incident angle  $7^\circ$  away from the normal to the surface, because the interaction of the implanted  $\text{Si}^+$  ions with GaN should be weak due to the strong bonding of GaN materials [44]. Figure 2.16 shows the  $S$  parameter as a function of  $E$  for the Si-implanted GaN before and after annealing, respectively. The result of the as-grown GaN epitaxial layer is also shown. The annealing behavior of the defects in Si-implanted GaN seems to be similar with that of the defects in Ge- and Ge+N-implanted GaN, as reported in section 2.2. That is, the annealing behavior of the implantation-induced vacancy-type defects is classified into 3 stages for Si-implanted GaN. First, part of the defects introduced in the implanted region diffuses into the deeper-lying region of the GaN layer during the implantation, in which the sample is estimated to be heated at about  $80^\circ\text{C}$ . Second, the size of the implantation-introduced defects increases gradually in both the implanted and deeper-lying regions with increasing annealing temperatures. At last, Si-related vacancy-type defects with marked different characters

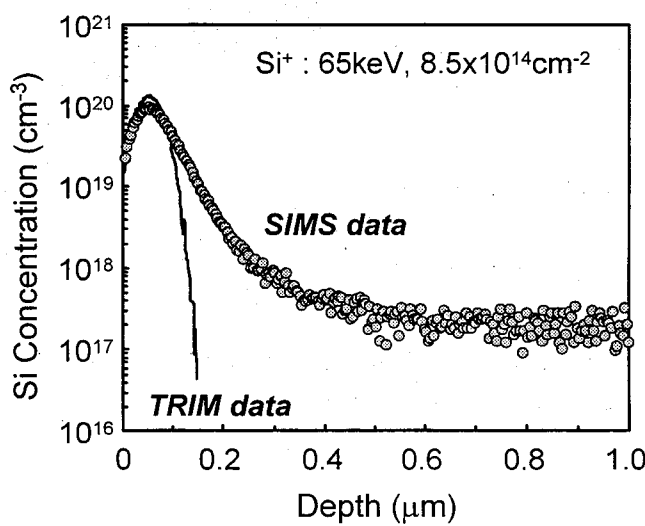


**FIG 2.15.** TRIM-simulated atomic profiles of implanted Si and SIMS profile of Si implanted GaN before annealing.

are newly created in the implanted region by the annealing above 900 °C. Bearing in mind that the electrical activation of the implanted Si atoms starts to occur after annealing at 1200 °C, these new vacancy-type defects are found to be created even at relatively low annealing-temperatures in which the implanted Si atoms have not yet be activated electrically. Additionally, the implantation-introduced defects are found to be immobile under all the annealing conditions.

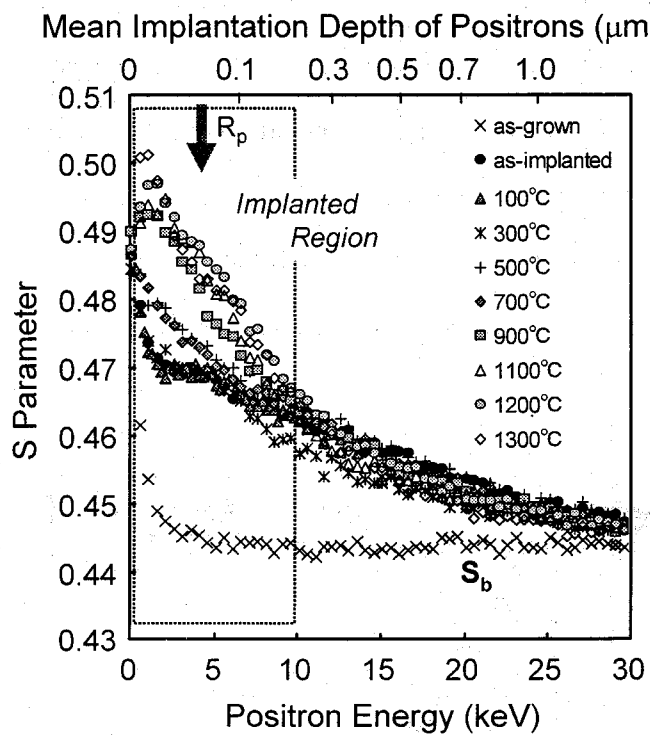


**FIG 2.16.**  $S$  parameter as a function of incident positron energy for Si-implanted GaN after annealing at various temperatures

In summary, we have demonstrated that the Si+N co-implantation into GaN and subsequent annealing at high temperatures can enhance the actual Si electrical activation based on a site-competition effect compared to the conventional Si implantation. In particular, overlapping of the N-implanted region with the Si one

makes the Si activation and crystallinity higher. The sheet carrier concentration is found to be precisely controllable between  $3 \times 10^{12} \text{ cm}^{-2}$  and  $5 \times 10^{14} \text{ cm}^{-2}$  with the Si activation efficiencies of ~50%. From AFM observations, Ga islands are found to be formed in surface region for the conventional Si-implanted GaN after the activation annealing, whereas the island formation is significantly suppressed in the case of the Si+N co-implantation. However, implantation-induced micro-defects can be seen to remain even after the high-temperature annealing process for both Si- and Si+N-implanted samples.

## 2.4 O Implantation

### 2.4.1 Experimental

The epitaxial GaN films used in these experiments were 2.5  $\mu\text{m}$  thick. They were grown on a-plane sapphire substrates by atmospheric pressure MOCVD at 1130 °C, with a pre-deposited 20 nm AlN buffer layer grown at 420 °C. The GaN films were not intentionally doped, but had a background n-type carrier concentration of  $\sim 5 \times 10^{15} \text{ cm}^{-3}$ . After growth, the GaN samples were implanted by using O<sub>2</sub> gas as the source of the <sup>16</sup>O<sup>+</sup> species. Prior to the O<sup>+</sup> implantation, a 100-nm-thick Ni layer was deposited on the top surface of the samples by electron-beam evaporation in order to reduce the implantation-induced damage. Then, multiple step O<sup>+</sup> implantation was performed as follows. The O<sup>+</sup> ions were implanted at 400, 300, 250, 200, 150, and 110 keV with dosages of  $4.5 \times 10^{14}$ ,  $8 \times 10^{13}$ ,  $1.2 \times 10^{14}$ ,  $1.3 \times 10^{14}$ ,  $7 \times 10^{13}$ , and  $1.5 \times 10^{14} \text{ cm}^{-2}$ , respectively, to produce a mean O concentration of  $2 \times 10^{19} \text{ cm}^{-3}$  to a depth of ~0.35  $\mu\text{m}$ . All of the implants were carried out at room temperature, with an incident angle 7° off the surface normal. After implantation, the Ni layer was removed and then a 500-nm-thick SiO<sub>2</sub> capping layer was deposited on the surface by radio-frequency sputtering at room temperature to provide an encapsulation cap for the subsequent implant activation anneal. All of the samples were annealed at temperatures between 1000 and 1200 °C for 5 min in flowing N<sub>2</sub> gas. Following the annealing step, HF was used to remove the SiO<sub>2</sub> cap, and then In contacts were formed at the corners of each sample. The O-doping characteristics were determined by variable temperature Hall-effect measurements, covering the temperature range from 16 to 300 K.

## 2.4.2 Results and Discussion

The depth distribution of the implanted O atoms was measured by SIMS. Figure 2.17 shows typical SIMS profiles of the implanted O atoms before and after annealing at 1100 °C, together with O atomic profiles calculated by TRIM code. Before the activation anneal, the O concentration to a depth of ~0.35 μm is confirmed to be about  $2 \times 10^{19} \text{ cm}^{-3}$ , as expected. The SIMS profiles of the implanted O atoms both before and after annealing are unchanged, in agreement with the profiles calculated by TRIM, regardless of annealing temperature. In other words, no measurable redistribution of the implanted O atoms is observed by the activation anneal. In addition, no Ni atoms were detected for all of the implanted samples. This suggests that the diffusion of Ni atoms into GaN from the Ni layer does not occur during the implantation process and consequently that the use of the Ni layer for reducing the implantation-induced damage does not influence the O-doping characteristics, as discussed later.

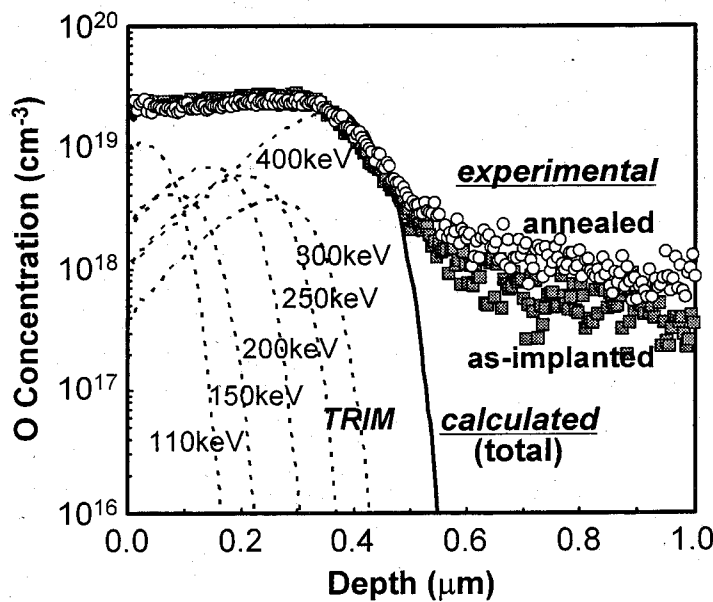


**FIG 2.17.** TRIM-simulated atomic profiles of implanted O and SIMS profiles of O implanted in GaN, as-implanted (■) and annealed (○) at 1100 °C.

The carrier type of the O-implanted GaN samples is confirmed to be an n-type under all of the annealing conditions. Figure 2.18 shows room-temperature sheet carrier concentration  $n_s$  and electron mobility  $\mu_e$  as a function of annealing temperature for the O-implanted samples. With the rise of annealing temperature from 1000 to 1100 °C, the  $n_s$  significantly increases from  $5.7 \times 10^{11}$  to  $1.1 \times 10^{13} \text{ cm}^{-2}$  with  $\mu_e$  of 83 - 141  $\text{cm}^2/\text{Vs}$ , respectively. This indicates that the O electrical activation starts to occur at around 1050 °C. On the other hand, the  $\mu_e$  significantly increases up to  $322 \text{ cm}^2/\text{Vs}$  in spite of the  $n_s$  being saturated by the annealing at 1200 °C. This behavior indicates an improvement in the crystallinity in the electrically activated region. Therefore, we can say that annealing at 1100 °C or higher temperatures is required to activate the implanted O atoms in GaN adequately. This critical temperature is in reasonable agreement with the previously reported value [21] and is relatively low compared to that of 1200 °C needed for the Si implantation doping. Here, the effective activation efficiency  $\eta_{eff}$  is defined as a ratio of the  $n_s$  to the total

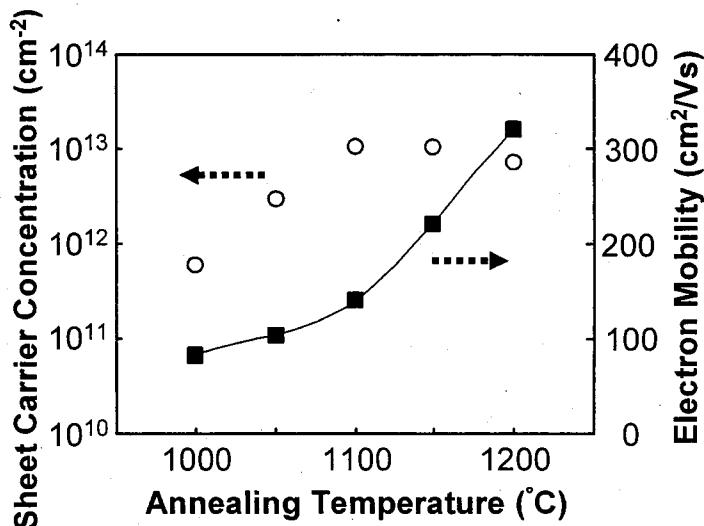


**FIG 2.18.** Sheet carrier concentration (○) and mobility (■) as a function of annealing temperature for O-implanted GaN samples.

dosages, assuming that all of the carriers are generated from the O donors. The  $\eta_{eff}$  is estimated to be only 1.1 % for the O-implanted GaN after annealing at 1100 °C. This value is extremely small compared to the  $\eta_{eff}$  of ~50 % in the case of the Si implantation doping, as reported in section 2.3.

Figure 2.19 shows typical Arrhenius plots of the  $n_s$  of the O-implanted GaN samples after annealing at 1000, 1100, and 1200 °C. All of the samples show carrier freeze out at low temperatures; its end temperature  $T_e$  shifts to higher temperatures with decreasing annealing temperature, which may be associated with the presence of the implantation-induced damage remained even after the activation annealing. At temperatures above  $T_e$ , the  $n_s$  tends to increase with the rise of temperature, regardless of annealing temperature. This implies thermal ionization of carriers from the O donor level. This ionization level is calculated to be ~18.3 meV from the slope of the line fitted to the Arrhenius plots for the activated GaN samples by 1100 and 1200 °C anneals. This value is close to the previously reported value [21,36]. Thus,

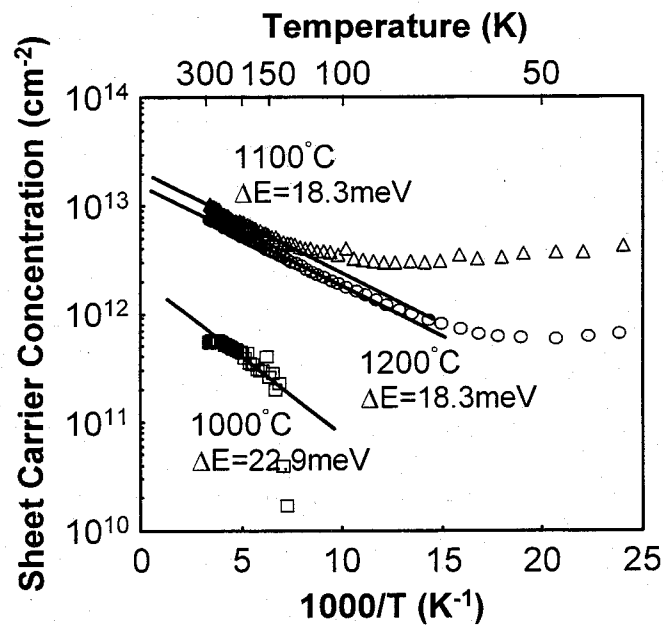


**FIG 2.19.** Arrhenius plots of sheet carrier concentration for O-implanted GaN samples after annealing at 1000, 1100, and 1200 °C.

the O donor level is very shallow and almost 100 % of the active donors can probably be ionized at room temperature. In addition, a cross-sectional value obtained by extracting from the fitted line strongly depends on annealing temperature; the value increases tenfold by 1100 and 1200 °C anneals compared to that in the case of a 1000 °C anneal. Bearing in mind that O atoms substitutionally incorporated into N sites can act as an O donor level [35], this value reflects the probability of the implanted O atoms occupying an N-lattice site in GaN. Therefore, we can say that few O atoms are present at N sites after a 1000 °C anneal, whereas the occupation probability increases significantly by the annealing at 1100 and 1200 °C. However, the O-implanted GaN displays an extremely low  $\eta_{eff}$  in spite of the O donor level being very shallow even after 1100 and 1200 °C anneals, as stated above. This result suggests that the majority of the implanted O atoms is present at an interstitial site in GaN and consequently has not contributed to the formation of the O donor level. In the meanwhile, from a practical point of view, the O<sup>+</sup> implantation doping with 1100 and 1200 anneals is probably effective in the formation of ohmic contacts to n-GaN for electronic devices regardless of the  $\eta_{eff}$  being low. In addition, some co-implantation techniques based on a site-competition effect may be required to improve the O-doping characteristics, as reported in sections 2.2 and 2.3 [23,29,30,32].

In summary, we have systematically investigated the dependence of the doping characteristics of the O-implanted GaN on annealing temperature. The implanted O atoms showed no measurable redistribution under the annealing conditions. The n-type activation of the O atoms started to occur after annealing at 1050 °C, but with a poor activation efficiency of only 1.1 %. Temperature dependence of the  $n_s$  revealed that O is a shallow donor with an ionization level of ~18.3 meV after 1100 and 1200 °C anneals. These experimental results can probably be caused by poor probability of the implanted O atoms occupying an N-lattice site in GaN.

## 2.5 Conclusion

Doping characteristics of Ge+N and Si+N co-implanted GaN have been systematically investigated. N-type regions were produced in undoped GaN films by the co-implantation and subsequent annealing with

an SiO<sub>2</sub> encapsulation layer at high temperatures. The annealing procedures above 1300 and 1200 °C were required to achieve an n-type activation for Ge+N and Si+N co-implanted GaN, respectively. Si activation efficiency of ~50 % has been achieved, which value is higher than Ge activation efficiency (~44 %) even after annealing at 1300 °C. This is probably due to the different behaviors of implantation-induced damage between them. Moreover, doping characteristics of O-implanted GaN have been investigated systematically from a viewpoint of annealing temperature. The implanted O atoms became electrically active as an n-type dopant after annealing above 1050 °C, but with a low activation efficiency of only 1.1 %.

## References

- [1] H. Morkoç, S. Strite, G. B. Gao, M. E. Lin, B. Sverdlov, and M. Burns, *J. Appl. Phys.* **76**, 1363 (1994).
- [2] T. P. Chow and R. Tyagi, *IEEE Trans. Electron Devices* **41**, 1481 (1994).
- [3] M. A. Khan, J. N. Kuznia, A. R. Bhattacharai, and D. T. Olson, *Appl. Phys. Lett.* **62**, 1786 (1993).
- [4] S. C. Binari, L. B. Rowland, W. Kruppa, G. Kelner, K. Doverspike, and D. K. Gaskill, *Electron. Lett.* **30**, 1248 (1994).
- [5] M. A. Khan, A. Bhattacharai, J. N. Kuznia, and D. T. Olson, *Appl. Phys. Lett.* **63**, 1214 (1993).
- [6] J. C. Zolper, R. J. Shul, A. G. Baca, R. G. Wilson, S. J. Pearton, and R. A. Stall, *Appl. Phys. Lett.* **68**, 2273 (1996).
- [7] F. Ren, M. Hong, S. N. G. Chu, M. A. Marcus, M. J. Schurman, A. Baca, S. J. Pearton, and C. R. Abernathy, *Appl. Phys. Lett.* **73**, 3893 (1998).
- [8] A. P. Zhang, J. W. Johnson, F. Ren, J. Han, A. Y. Polyakov, N. B. Smirnov, A. V. Govorkov, J. M. Redwing, K. P. Lee, and S. J. Pearton, *Appl. Phys. Lett.* **78**, 823 (2001).
- [9] A. P. Zhang, G. Dang, F. Ren, J. Han, A. Y. Polyakov, N. B. Smirnov, A. V. Govorkov, J. M. Redwing, H. Cho, and S. J. Pearton, *Appl. Phys. Lett.* **76**, 3816 (2000).
- [10] J. Kim, R. Mehandru, B. Luo, F. Ren, B. P. Gila, A. H. Onstine, C. R. Abernathy, S. J. Pearton, and Y. Irokawa, *Appl. Phys. Lett.* **80**, 4555 (2002).

- [11] J. Kim, R. Mehandru, B. Luo, F. Ren, B. P. Gila, A. H. Onstine, C. R. Abernathy, S. J. Pearton, and Y. Irokawa, *Appl. Phys. Lett.* **81**, 372 (2002).
- [12] S. J. Pearton, C. B. Vartuli, J. C. Zolper, C. Yuan, and R. A. Stall, *Appl. Phys. Lett.* **67**, 1435 (1995).
- [13] J. C. Zolper, H. H. Tan, J. S. Williams, J. Zou, D. J. H. Cockayne, S. J. Pearton, M. H. Crawford, and R. F. Karlicek, Jr., *Appl. Phys. Lett.* **70**, 2729 (1997).
- [14] X. A. Cao, C. R. Abernathy, R. K. Singh, S. J. Pearton, M. Fu, V. Sarvepalli, J. A. Sekhar, J. C. Zolper, D. J. Rieger, J. Han, T. J. Drummond, R. J. Shul, and R. G. Wilson, *Appl. Phys. Lett.* **73**, 229 (1998).
- [15] C. J. Eiting, P. A. Grudowski, R. D. Dupuis, H. Hsia, Z. Tang, D. Becher, H. Kuo, G. E. Stillman, and M. Feng, *Appl. Phys. Lett.* **73**, 3875 (1998).
- [16] J. A. Fellows, Y. K. Yeo, R. L. Hengehold, and D. K. Johnstone, *Appl. Phys. Lett.* **80**, 1930 (2002).
- [17] J. K. Sheu, C. J. Tun, M. S. Tsai, C. C. Lee, G. C. Chi, S. J. Chang, and Y. K. Su, *J. Appl. Phys.* **91**, 1845 (2002).
- [18] J. K. Sheu, M. L. Lee, L. S. Yeh, C. J. Kao, C. J. Tun, M. G. Chen, G. C. Chi, S. J. Chang, Y. K. Su, and C. T. Lee, *Appl. Phys. Lett.* **81**, 4263 (2002).
- [19] D. G. Kent, M. E. Overberg, and S. J. Pearton, *J. Appl. Phys.* **90**, 3750 (2002).
- [20] J. S. Chan, N. W. Cheung, L. Schloss, E. Jones, W. S. Wong, N. Newman, X. Liu, E. R. Weber, A. Gassman, and M. D. Rubin, *Appl. Phys. Lett.* **68**, 2702 (1996).
- [21] J. C. Zolper, R. G. Wilson, S. J. Pearton, and R. A. Stall, *Appl. Phys. Lett.* **68**, 1945 (1996).
- [22] H. Kobayashi and W. H. Gibson, *Appl. Phys. Lett.* **74**, 2355 (1999).
- [23] J. Y. Nakano, R. K. Malhan, T. Kachi, and H. Tadano, *J. Appl. Phys.* **89**, 5961 (2001).
- [24] R. Krause-Rehberg and H. S. Leipner, in *Positron Annihilation in Semiconductors: Defect studies* (Springer-Verlag, Berlin, 1999).
- [25] K. Saarinen, T. Laine, S. Kuima, J. Nissila, P. Hautojarvi, L. Dobrzynski, J. M. Baranowski, K. Pakula, R. Stepniewski, M. Wojdak, A. Wysmolek, T. Suski, M. Leszczynski, I. Grzegory, and S. Porowski, *Phys. Rev. Lett.* **79**, 3030 (1997).

- [26] K. Saarinen, P. Seppala, J. Oil, P. Hautojarvi, C. Corbel, O. Briot, and R. L. Aulombard, *Appl. Phys. Lett.* **73**, 3253 (1998).
- [27] J. Oil, V. Ranki, J. Kivioja, K. Saarinen, P. Hautojarvi, J. Likonen, J. M. Baranowski, K. Pakula, T. Suski, M. Leszczynski, and I. Grzegory, *Phys. Rev. B* **63**, 45205 (2001).
- [28] A. Uedono, S. F. Chichibu, Z. Q. Chen, M. Sumiya, R. Suzuki, T. Ohdaira, T. Mikado, T. Mukai, and S. Nakamura, *J. Appl. Phys.* **90**, 181 (2001).
- [29] Y. Nakano, T. Kachi, and T. Jimbo, *Jpn. J. Appl. Phys.* **41**, 2522 (2002).
- [30] Y. Nakano and T. Jimbo, *J. Appl. Phys.* **92**, 3815 (2002).
- [31] Y. Nakano and T. Jimbo, *Appl. Phys. Lett.* **81**, 3990 (2002).
- [32] Y. Nakano, T. Kachi, and T. Jimbo, *Appl. Phys. Lett.* **82**, 2082 (2003).
- [33] D. K. Gaskill, N. Bottka, and M. C. Lin, *Appl. Phys. Lett.* **28**, 1449 (1986).
- [34] B-C. Chung and M. Gershenson, *J. Appl. Phys.* **72**, 651 (1992).
- [35] H. Sato, T. Minami, E. Yamada, M. Ishii, and S. Takata, *J. Appl. Phys.* **75**, 1405 (1994).
- [36] W. J. Moore, J. A. Freitas Jr., G. C. B. Braga, R. J. Molnar, S. K. Lee, K. Y. Lee, and I. J. Song, *Appl. Phys. Lett.* **79**, 2570 (2001).
- [37] Y. Nakano, T. Kachi, and T. Jimbo, *J. Vac. Sci. Technol. B* **21**, 2602-2604 (2003).
- [38] P. Hautojarvi and C. Corbel, in *Positron Spectroscopy of Solids*, edited by A. Dupasquier and A. P. Mills, Jr. (IOS Press, Amsterdam, 1995).
- [39] W. Götz, N. M. Johnson, H. Amano, and I. Akasaki, *Appl. Phys. Lett.* **65**, 463 (1994).
- [40] P. Boguslawski, E. L. Briggs, and J. Bernholc, *Phys. Rev. B* **51**, 17255 (1995).
- [41] U. Myler and P. J. Simpson, *Phys. Rev. B* **56**, 14303 (1997).
- [42] J. Neugebauer and C. G. Van de Walle, *Appl. Phys. Lett.* **69**, 503 (1996).
- [43] A. Uedono and Y. Nakano, (unpublished).
- [44] *private communications* with O. Eryu and A. Uedono.